

Chapter 3

Optical properties of nanostructures

References: *lecture notes by Prof. Oliver Benson, TU Berlin (2009);*
L. Novotny, B. Hecht, Principles of Nano-Optics, Cambridge University Press (2006);
S. A. Maier, Plasmonics: Fundamentals and Applications, Springer (2007)

In the transition from macroscopic structures to nanostructures, the optical properties of materials can change dramatically. For example, the density of states of semiconductor quantum dots forms a discrete energy level system, whereby light emitted by such quantum dots also assumes discrete energy values. By nanostructuring bulk materials on the sub-wavelength scale, photonic bandgaps can be induced in analogy to electronic bandstructures (\rightarrow photonic crystals), or refractive indices with a negative real part can be realized (\rightarrow metamaterials). At the interface between metals and dielectrics surface plasmons can be excited, which can be used to focus light at the location of nanotips to dimensions far below the diffraction limit. In metal nanostructures particle plasmons can be excited that are accompanied by resonance effects, which change the observed colour of the particles and lead to an enhancement of the electrical near-field by many orders of magnitude. Such modified optical properties open up new possibilities for investigating fundamental light-matter-interactions as well as for nano-optical applications.

Key questions of modern optics are concerned with effects on the nanoscale, such as:

- How can we obtain information on structure and function on a scale below 100 nm using optical methods?
- What are the relevant processes in light-matter-interaction (from classical to quantum mechanical)?
- What are the fundamental limitations of the “optical” description of phenomena on the nanoscale?

Out of the investigation of optical effects on the nanoscale, research areas such as **nano-optics**, **nano-phononics**, **nano-plasmonics** or **nano-spectroscopy** have emerged.

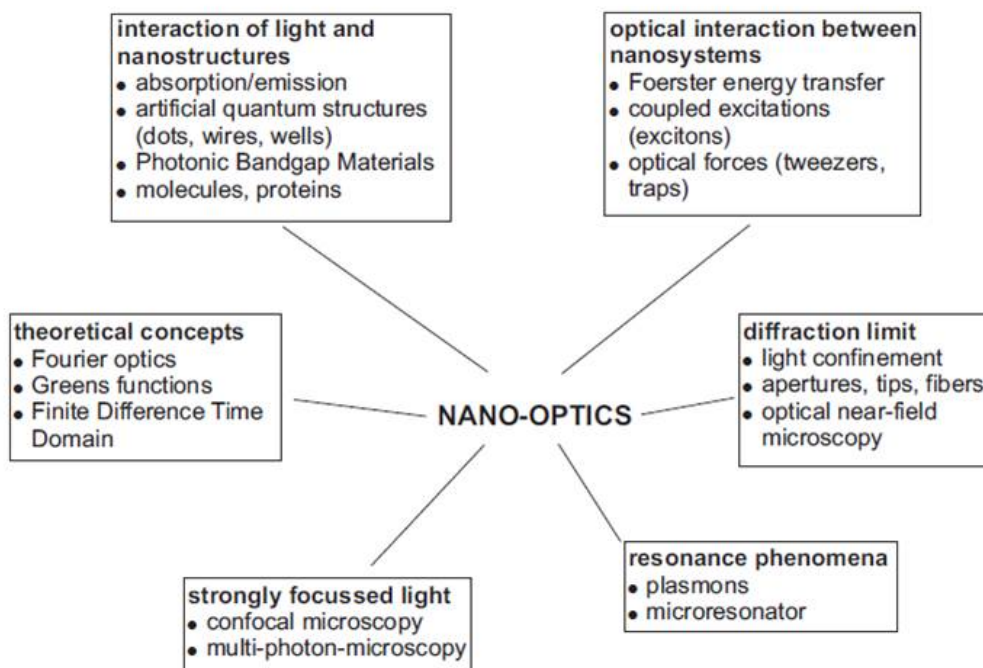


Fig. 3.1: Modern areas of nano-photonics [Lecture notes, O. Benson, TU Berlin]

Prerequisite for addressing the respective research questions is a highly advanced state of technology, including suitable nanofabrication and synthesis, instrumentation development, and optical methods, see ch. 6 and 7.

Today's modern optics already provides very powerful analytical techniques, offering ultra-high optical spatial resolution (down to less than 10 nm), relative precisions of $< 10^{-17}$, temporal resolution (femtoseconds and less, \rightarrow *ultrafast optics*), spectral resolution ($< 1 \text{ cm}^{-1}$), and sensitivity down to single molecule detection.

Some areas of nano-optics and nano-photonics are highlighted in Fig. 3.1.

Current active research topics include:

- Theory of electromagnetic fields and light-matter-interaction
- Optical interactions (energy transfer etc.) between nanostructures
- Plasmons (surface plasmons and localized surface plasmons) and plasmon resonances
- Focussing of light beyond the diffraction limit
- Single molecule spectroscopy
- Superresolution imaging (STED, STORM/PALM, ...; Nobel Prize in chemistry 2014)
- Near-field techniques (SNOM, TERS, ...)
- Nanostructuring and synthesis of nanostructured materials
- Photonic crystals (modification of the photonic band structure)
- Metamaterials (optical cloaking, modification of the dielectric function)
- Quantum emitters and single photon sources
- ...

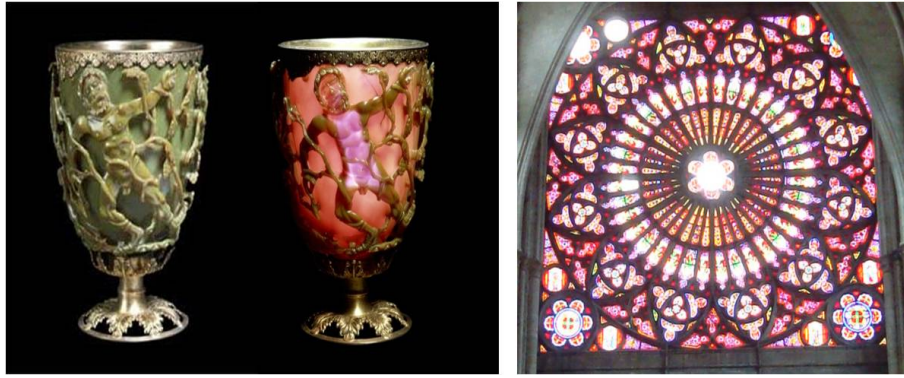


Fig. 3.2: Early examples of the colour effects of metallic nanoparticles: (a) Lycurgus cup (4th century B.C.), (b) medieval church windows, Troyes, France [www.britishmuseum.org, archive M. Fleischer]

3.1 Plasmonics

In **plasmonics** the interactions between electromagnetic waves, especially of light in the UV/visible/near-infrared range, with metallic interfaces, films and metal nanoparticles (especially noble metals) are investigated.

Although research into the interaction between visible light and metal structures has strongly intensified over the last century, prominent effects of light-metal particle-interaction have been phenomenologically known for many centuries. Figure 3.2 illustrates the colour effects of metal particles embedded in glass that were already harnessed in the antique and middle ages. Descriptions of the observed phenomena were developed e.g. 1908 by Gustav Mie (scattering processes) and 1957 by Rufus Ritchie (plasmons). The theory of *bulk plasmons* (3D), *surface plasmon polaritons* (2D, 1D), and *localized surface plasmon polaritons* (nanostructures) is based on the fundamentals of electrodynamics.

The interaction of metals with electro-magnetic fields can be fully described within the framework of the classical **Maxwell equations**:

$$\nabla \cdot \mathbf{D} = \rho \quad (3.1)$$

$$\nabla \cdot \mathbf{B} = 0 \quad (3.2)$$

$$\nabla \times \mathbf{E} = -\partial \mathbf{B} / \partial t \quad (3.3)$$

$$\nabla \times \mathbf{H} = \mathbf{J} + \partial \mathbf{D} / \partial t \quad (3.4)$$

which connect the macroscopic fields (dielectric displacement \mathbf{D} , electric field \mathbf{E} , magnetic field \mathbf{H} and magnetic induction \mathbf{B}) with an external charge density ρ and current density \mathbf{J} .

In the limit of linear, isotropic and non-magnetic ($\mu = 1$) media, the following **constitutive relations** also hold:

$$\mathbf{D} = \epsilon_0 \epsilon \mathbf{E} \quad (3.5)$$

$$\mathbf{B} = \mu_0 \mathbf{H} \quad (3.6)$$

with a **frequency dependent dielectric function (complex permittivity)**

$$\epsilon = \epsilon(\omega) = \epsilon' + i\epsilon'' \quad (3.7)$$

It is furthermore connected to the **complex index of refraction** via

$$n_c(\omega) = n + i\kappa = \sqrt{\epsilon} \quad (3.8)$$

Explicitly one can obtain the following expressions for the real and imaginary parts:

$$\epsilon' = n^2 - \kappa^2, \quad \epsilon'' = 2n\kappa \quad (3.9)$$

$$n^2 = \frac{\epsilon'}{2} + \frac{1}{2}\sqrt{\epsilon'^2 + \epsilon''^2}, \quad \kappa = \frac{\epsilon''}{2n} \quad (3.10)$$

The real part of the refractive index, $n(\omega)$, is responsible for the **dispersion** in the medium, the imaginary part, $\kappa(\omega)$ (extinction coefficient), determines the **absorption**. **Beer's law** describes the exponential decay of the intensity of a light beam (along the x -direction) in a medium:

$$I(x) = I_0 e^{-\alpha x} \quad (3.11)$$

The absorption constant α can then be determined from the extinction coefficient:

$$\alpha(\omega) = 2\kappa(\omega)\omega/c. \quad (3.12)$$

3.2 Bulk plasmons

The optical properties can be described over a large frequency range using the *plasma model*, where an electron gas (effective electron mass m) of density N is assumed that moves freely on a background of positively charged atom cores. These electrons are excited to form oscillations in the presence of an electromagnetic field $\mathbf{E}(t) = \mathbf{E}_0 \exp(-i\omega t)$, which are damped through collisions with a characteristic rate $\gamma = 1/\tau$ (typically $\tau \simeq 10^{-14}$ s at room temperature). The equations of motion in this model are

$$m\ddot{\mathbf{x}} + m\gamma\dot{\mathbf{x}} = -e\mathbf{E}(t) \quad (3.13)$$

with the solution

$$\mathbf{x}(t) = \frac{e}{m(\omega^2 + i\gamma\omega)}\mathbf{E}(t) \quad (3.14)$$

The electrons that are displaced relative to the atom cores then generate a polarisation $\mathbf{P} = -Nex$. For the dielectric displacement and the permittivity, it follows:

$$\mathbf{D} = \epsilon_0\mathbf{E} + \mathbf{P} = \epsilon_0\epsilon\mathbf{E} = \epsilon_0\left(1 - \frac{\omega_p^2}{\omega^2 + i\gamma\omega}\right)\mathbf{E} \quad (3.15)$$

$$\Rightarrow \epsilon(\omega) = 1 - \frac{\omega_p^2}{\omega^2 + i\gamma\omega} = 1 - \frac{\omega_p^2\tau^2}{\omega^2\tau^2 + i\omega\tau} \quad (3.16)$$

where the **plasma frequency** ω_p with $\omega_p^2 = \frac{Ne^2}{\epsilon_0 m}$ is introduced.

If electrostatic screening is taken into account, the above equation is modified to

$$\epsilon(\omega) = \epsilon_\infty - \frac{\omega_p^2}{\omega^2 + i\gamma\omega} \quad (3.17)$$

with a constant value ϵ_∞ .

In the case of low frequencies $\omega\tau \ll 1$ metals are strongly absorbing and become opaque. The absorption constant then becomes $\alpha = \sqrt{2\omega_p^2\omega\tau/c^2}$. The penetration depth of the fields into metal at low frequencies corresponds to $\delta = 1/\alpha$ according to Beer's law and is denoted as the **skin depth**.

In the case of large frequencies the approximation $\omega\tau \gg 1$ is valid. In this case the damping term $i\omega\tau$ can be neglected, and $\epsilon(\omega)$ becomes approximately real:

$$\epsilon(\omega) = 1 - \frac{\omega_p^2}{\omega^2} \quad (3.18)$$

The **dispersion relation** of electro-magnetic fields can be determined from $k^2 = |\mathbf{k}|^2 = \epsilon\omega^2/c^2$ to:

$$\omega(k) = \sqrt{\omega_p^2 + k^2 \cdot c^2} \quad (3.19)$$

In Fig. 3.3 the dispersion relation $\omega(k)$ of bulk plasmons is shown. As can be seen, no propagation of electro-magnetic waves takes place below the plasma frequency, $\omega < \omega_p$. For $\omega > \omega_p$ waves propagate with a group velocity of $v_g = d\omega/dk < c$.

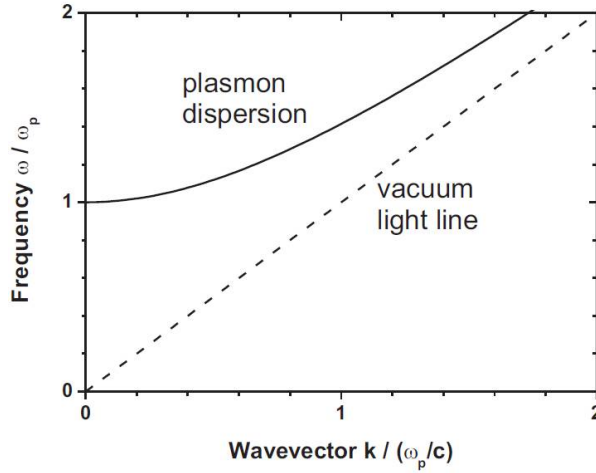


Fig. 3.3: Dispersion relation of the free electron gas [O. Benson, TU Berlin]

Of further interest is the special case $\omega = \omega_p$, where for low damping $\epsilon(\omega_p) \simeq 0$. One can show (see S. Maier “Plasmonics”, p. 10 and 15f.) that here a collective longitudinal excitation mode ($\mathbf{k} \parallel \mathbf{E}$) is formed, with a purely depolarizing field $\mathbf{E} = -\epsilon_0^{-1}\mathbf{P}$. The physical interpretation is a collective oscillation of the conduction electron gas relative to the fixed background of positive atom cores. The **quanta of this charge**

oscillation are called **plasmons** (or **bulk plasmons**, for better distinction from the *surface plasmons* discussed in the following sections). As these are longitudinal waves, bulk plasmons cannot couple to transversal electro-magnetic fields, and thus cannot be excited by direct illumination or coupled out as light.

For most metals the plasma frequency is in the ultra-violet regime, with energies in the range 5-15 eV, depending on the metal band structure.

3.3 Surface plasmons

Surface plasmons (short for **surface plasmon polaritons, SPPs**) are electro-magnetic excitations that can propagate along the interface between a metal and a dielectric medium, respectively charge density oscillations that couple with the incoming light field.

To derive these excitations, we start again from Maxwell's equations, which for the case of an interface need to be separately solved for the metal and dielectric parts. The starting point is a metal surface that extends infinitely in the x - y -plane at $z = 0$ (see Fig. 3.4).

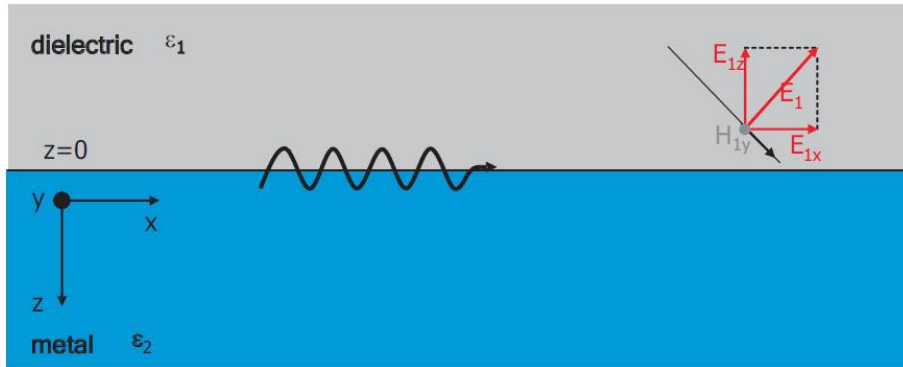


Fig. 3.4: Schematic interface along the x - y -plane between a dielectric (index 1) and metal (index 2) [Lecture notes, O. Benson, TU Berlin]

The conditions of continuity for the perpendicular and transversal field components at this interface (see e.g. J.D. Jackson, “Classical Electrodynamics”) are given by

$$D_{1,z} = D_{2,z}, \quad B_{1,z} = B_{2,z} \quad (3.20)$$

$$E_{1,x/y} = E_{2,x/y}, \quad H_{1,x/y} = H_{2,x/y} \quad (3.21)$$

where the indices (1) and (2) indicate the dielectric and metal, respectively.

It can be shown (see e.g. S. Maier “Plasmonics”, p. 26f.) that under these conditions no tranverse-electric modes (TE modes, no electric field in the direction of propagation) can exist. Instead we directly start with an ansatz for a transverse-magnetic mode (TM mode, no magnetic field in the direction of propagation) for fields which propagate along the x -direction ($j = 1, 2$):

$$\mathbf{E}_j = (E_{j,x}, 0, E_{j,z})e^{i(\mathbf{k}_j \mathbf{r} - \omega t)} \quad (3.22)$$

$$\mathbf{H}_j = (0, H_{j,y}, 0)e^{i(\mathbf{k}_j \mathbf{r} - \omega t)} \quad (3.23)$$

$$\mathbf{D}_j = \epsilon_0 \epsilon_j \mathbf{E}_j, \quad \mathbf{B}_j = \mu_0 \mathbf{H}_j \quad (3.24)$$

The wave vector is given by $\mathbf{k}_j = (\beta, 0, k_{j,z})$, where $\beta = k_x$ indicates the constant propagation along x .

Using this approach with the conditions of continuity from above and the Maxwell's equations in the absence of charges and currents ($\rho = 0, \mathbf{J} = 0$), one obtains the following relations between the $k_{j,z}$ components:

$$\frac{k_{1,z}}{\epsilon_1} = \frac{k_{2,z}}{\epsilon_2} \quad (3.25)$$

For solutions that describe modes bound to the interface (i.e. no propagating components in $k_{j,z}$ -direction), the $k_{j,z}$ components have to be imaginary and of opposite signs, since they belong to the different half-spaces:

$$k_{1,z} = +i\kappa_1; \quad k_{2,z} = -i\kappa_2 \quad (3.26)$$

The fields thus decay exponentially into the respective half spaces: $\mathbf{E}_j \propto e^{\pm i k_{j,z} z} = e^{\pm \kappa_j z}$ (with κ_j real) as schematically shown in Fig. 3.5. These **evanescent fields** are therefore localized very close to the surface and are denoted as **electrical near-fields**. From the above equations one can directly see that these conditions are fulfilled only if the real parts of the dielectric functions of the two materials are of opposite sign (i.e. $\epsilon'_1 = -\epsilon'_2$). Surface plasmons can thus indeed only exist at the interface between a metal ($\epsilon' < 0$) and a dielectric medium ($\epsilon' > 0$).

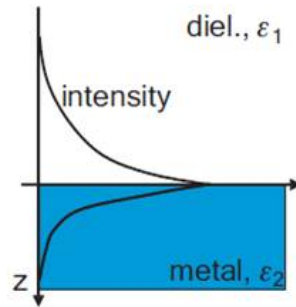


Fig. 3.5: Schematic of evanescent fields that decay exponentially into the two half-spaces [Lecture notes O. Benson, TU Berlin]

Altogether one obtains a system that is composed of an electro-magnetic wave in the dielectric medium and an oscillating electron plasma in the metal, where both modes have an exponentially decaying evanescent character (cf. Fig. 3.6). Due to this composite character, surface plasmons are fully denoted as surface plasmon polaritons. The penetration depth of the electric field into the dielectric is typically on the order of $\lambda/2$ of the wavelength in the medium, whereas the penetration depth in the metal is characteristically given by the skin depth δ (on the order of few 10 nm for metals at optical frequencies).

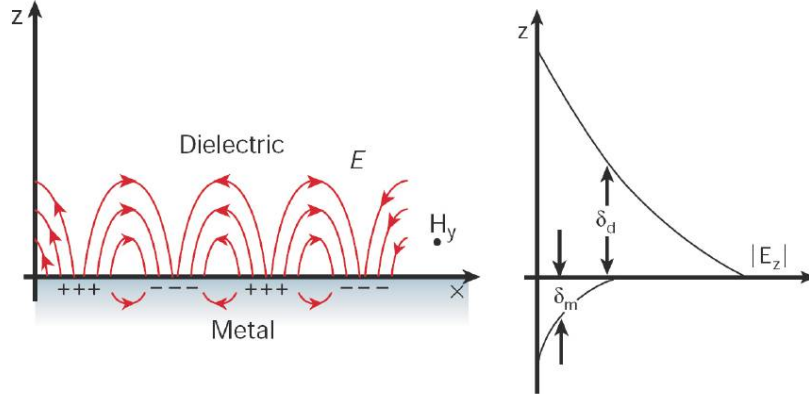


Fig. 3.6: Left: composite character of SPPs consisting of an electromagnetic wave and a charge density oscillation at the interface between dielectric and metal; right: evanescent fields with their respective penetration depths in the two half-spaces [Barnes et al., Nature 424, 824 (2003)]

The **dispersion relation for surface plasmons** can be derived from the wave vectors:

$$|\mathbf{k}_{1/2}|^2 = \epsilon_{1/2} k_0^2 = \beta^2 + k_{1/2,z}^2 = \beta^2 - \kappa_{1/2}^2 \quad (3.27)$$

where $k_0 = \omega/c$ is the vacuum wave vector of light with frequency ω . Insertion of $\kappa_{1/2}$ into the equation $k_{1,z}/\epsilon_1 = k_{2,z}/\epsilon_2$ yields the propagation constant

$$\beta = k_x = \frac{\omega}{c} \sqrt{\frac{\epsilon_1 \epsilon_2}{\epsilon_1 + \epsilon_2}} \quad (3.28)$$

If the frequency dependencies $\epsilon_{1,2}(\omega)$ are known, this equation can be solved for ω to obtain the dispersion relation $\omega(k_{SPP})$.

Under the assumption that $\epsilon_1(\omega)$ in the dielectric is approximately constant, and using the low-damping approximation $\epsilon_2(\omega) \simeq 1 - \omega_p^2/\omega^2$ for ϵ_2 in the metal, one obtains a dispersion relation as shown in Fig. 3.7.

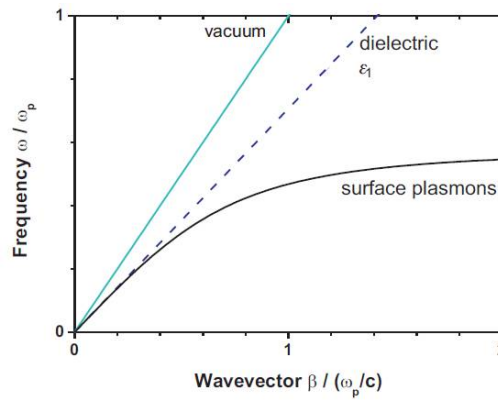


Fig. 3.7: Dispersion relation of surface plasmons compared to light in vacuum and in a dielectric medium [Lecture notes O. Benson, TU Berlin]

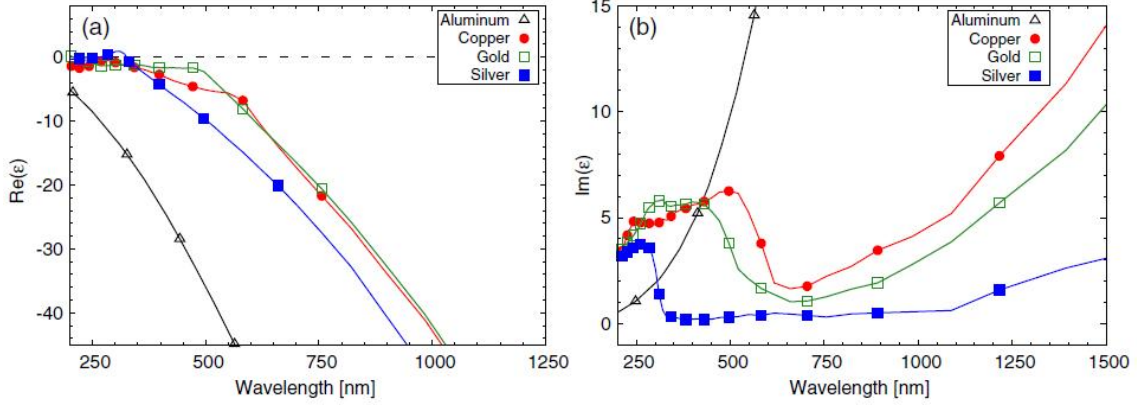


Fig. 3.8: (a) Real and (b) imaginary parts of the complex dielectric functions for Al, Cu, Au and Ag. For plasmonic applications, the real part has to be negative; for low-loss operation, the imaginary part needs to be small [N.C. Lindquist et al., Rep. Prog. Phys. 75, 036501 (2012)]

It can clearly be seen that the SPP dispersion relation remains entirely below the light cone, while a coincidence only occurs in the limit $\omega = 0, \beta = 0$. SPPs thus cannot be excited by direct illumination with light, as energy and momentum conservation ($\omega_{\text{light}} = \omega_{\text{SPP}}$ and $\mathbf{k}_{\text{light}} = \mathbf{k}_{\text{SPP}}$) cannot be fulfilled at the same time. Instead, in order to excite SPPs, an additional momentum transfer has to be induced. Techniques for meeting this requirement will be discussed below.

The components normal to the surface that decay into the dielectric ($j = 1$) and the metal ($j = 2$) can be calculated to

$$k_{j,z}^2 = \frac{\epsilon_j^2}{\epsilon_1 + \epsilon_2} k_0^2. \quad (3.29)$$

In the above discussion, the complex nature of the dielectric function of the metal was not yet considered. Figure 3.8 shows the real and imaginary parts of the complex permittivities for some selected metals. The imaginary part of the dielectric function causes Ohmic damping of the electron oscillations in the metal. From the above equation for β , one sees that the propagation constant is also a complex function, $\beta = \beta' + i\beta''$.

N.B.: Note that the square root of a complex number $a + ib$ can be calculated by:

$$\sqrt{a + ib} = \sqrt{\frac{\sqrt{a^2 + b^2} + a}{2}} + i \operatorname{sgn}(b) \sqrt{\frac{\sqrt{a^2 + b^2} - a}{2}} \quad (3.30)$$

As a consequence, in the solutions for the SPPs $\mathbf{E}_2 = (E_{2,x}, 0, E_{2,z}) \exp(i\mathbf{k}_2 \mathbf{r} - i\omega t)$, an exponentially decaying damping term $\exp(-\beta'' x)$ occurs, which results in a characteristic propagation length for the intensity of the SPPs given by

$$\delta_{\text{SPP}} = \frac{1}{2\operatorname{Im}(\beta)} = \frac{1}{2\beta''} \quad (3.31)$$

Typical ranges of the SPPs are on the order of a few micrometers at visible wavelengths and up to few 100 μm in the infrared.

This situation changes in the case of metal films of thickness d , which offer two interfaces to dielectric substrates. In the case of a thick metal film on a dielectric substrate, two independent SPP modes exist, depending on the different dielectric constants of the media adjacent to the metal interfaces. These modes will be degenerate if the film is surrounded by a symmetrical environment. If a metal film is sufficiently thin such that the electro-magnetic interaction between the interfaces can no longer be neglected, the SPP dispersion is significantly modified, and coupling between the SPP modes at the different interfaces of the film takes place. Through the interaction of the SPP modes the degeneracy of the spectrum is lifted, and the surface plasmon frequencies split into two branches corresponding to a symmetric (low-frequency) mode and an antisymmetric (high-frequency) mode. For large SPP wave vectors these modes can be estimated to

$$\omega_{\pm} = \omega_{SPP} \sqrt{1 \pm \exp(-\beta d)} \quad (3.32)$$

At the same time, for such thin metal films the imaginary part of the wave vector determining the propagation length of the high-frequency SPP modes decreases $\propto d^2$ with the film thickness. This leads to a very long propagation length of such SPP modes, which are called **long-range SPPs**. These modes can have propagation lengths up to centimeters in the infrared regime.

Configurations for the excitation of surface plasmon polaritons:

As shown in the previous section, the SPP dispersion curve resides entirely below that of free space light in vacuum, such that $\beta > k$. Direct excitation of SPPs by light is therefore only possible if special techniques are employed to achieve phase matching. Effective coupling schemes include the following (see Fig. 3.9):

- Prism coupling: Light is coupled in from the back via a prism that is coated with a thin metal film (Kretschmann configuration) or couples to a metal film via a small air gap (Otto configuration).
- Grating coupling: Phase matching is ensured by a grating on the surface, with $\beta = k \sin \Theta \pm nG$, where Θ is the angle of incidence, $G = \frac{2\pi}{a}$ and a the grating period.
- Strongly focused light beams: By focusing a collimated beam, a large range of angles with different \mathbf{k} -vectors is presented at the surface.
- Near-field excitation: By positioning a metal film in the near-field of e.g. a metal tip, SPPs can be launched. The SPPs propagate radially away from the location of the excitation in the film.
- Coupling to photonic elements: Particularly in view of plasmonic optical devices, SPPs can be launched by coupling to wave guides or optical fibres.

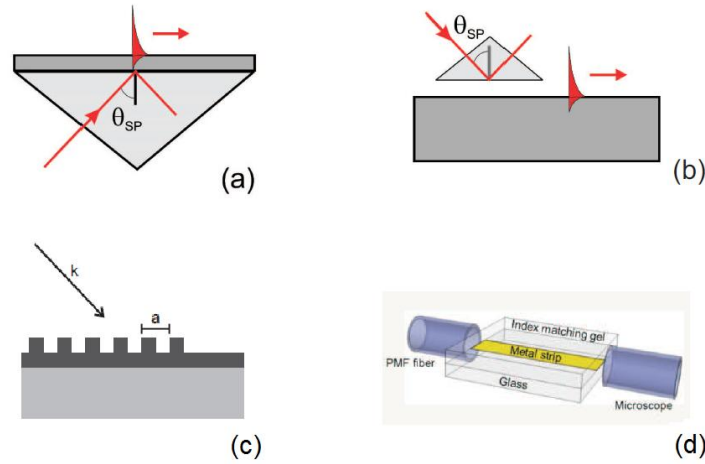


Fig. 3.9: Excitation of SPPs using (a) prism coupling in Kretschmann and (b) Otto configuration, (c) grating coupling, and (d) fibre coupling [(a,b) Zayats and Smolyaninov, J. Opt. A: Pure Appl. Opt. 5, S16S50 (2003), (c) lecture notes O. Benson, TU Berlin, (d) http://people.ee.duke.edu/~drsmith/plasmon_waveguides.htm]

“1D” surface plasmons

By further restricting the sample dimensions, “1D” surface plasmons can be excited. They can e.g. propagate along waveguides or metal nanowires (cf. Fig. 3.10). Coupled SPP modes may be formed in dielectric/metal/dielectric (*insulator-metal-insulator*, *IMI*) or metal/dielectric/metal (*MIM*) structures, such as gaps, V-grooves or ridges. These structures give rise to interesting physical considerations as well as potential applications for optical devices, e.g. by waveguiding on an optical chip.

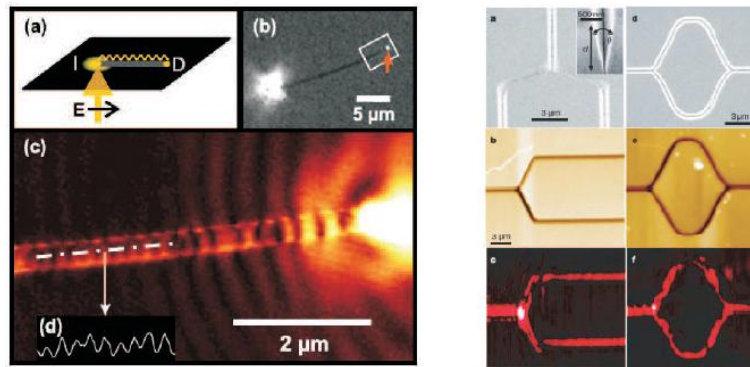


Fig. 3.10: Left: (a) SPP propagation along a nanowire; (b) microscopic and (c) near-field microscopic image of the propagating SPP, (d) cross-section along the dotted line. Right: Plasmonic Y-splitter and Mach-Zehnder interferometer realised by a V-groove that acts as a waveguide for SPPs, top to bottom: SEM, topography, and near-field images. [Ditlbacher et al., Phys. Rev. Lett. 95, 257403 (2005); Bozhevolnyi et al., Nature 440, 508 (2006)]

SPPs are non-radiative modes and cannot be directly observed e.g. in an optical microscope. They can however be visualized by scattering the electric near-field accompanying the SPPs to the far-field by scanning a sharp tip across the surface at a very close distance (\rightarrow SNOM). This technique was e.g. used in Fig. 3.10(left,c).

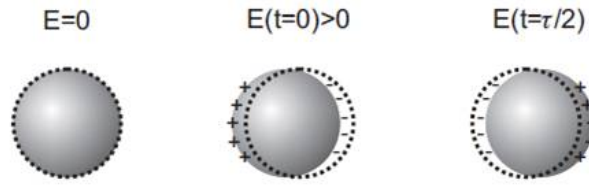


Fig. 3.11: Schematic of localized surface plasmons on a metal nanoparticle in the absence (left) and presence (center and right) of an oscillating external electro-magnetic field [Lecture notes, O. Benson, TU Berlin]

3.4 Localized surface plasmons (particle plasmons)

In metal particles with dimensions on the order of and below the wavelength of light, the collective oscillations of the free electron density are confined to the geometric dimensions of the nanostructures. This results in another type of fundamental plasmonic excitation, the **localized surface plasmon polaritons (LSPPs)**, also known as *particle plasmons*. LSPPs are non-propagating plasmon excitations localized on metallic nanostructures.

For small isolated metal particles with sizes in the range of the penetration depth of an electromagnetic field (skin depth ~ 20 nm for Ag in the optical range), the clear distinction between surface and bulk plasmon vanishes. An external field can penetrate into the volume and shift the conduction electrons with respect to the ion lattice (see Fig. 3.11). This results in a **dipole-like charge separation** (Fig. 3.11). The coherently shifted electrons together with the restoring field represent an oscillator, the behaviour of which is defined by the effective electron mass, charge density, and geometry of the particle. The oscillator undergoes a resonant behaviour, called **plasmon resonance** (see Fig. 3.12(a)). Most physical effects associated with LSPPs can be explained within this simple model. The plasmon resonances of noble metal particles, which are particularly well-suited for the observation of LSPPs, typically appear in the visible to near-infrared spectral range. At resonance, the amplitude of the induced electro-magnetic field (**enhanced near-field**) can exceed the exciting field strength by an order of magnitude.

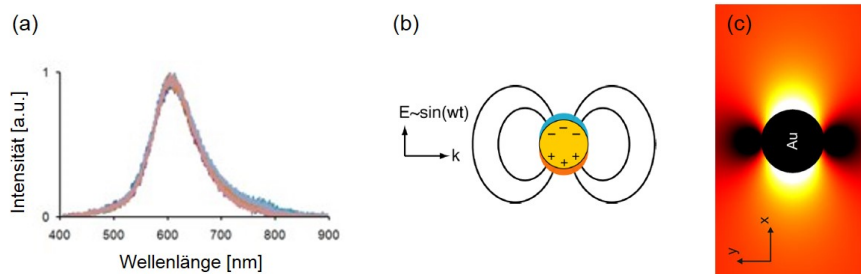


Fig. 3.12: (a) Plasmon resonance curves of the scattering intensity; (b) plasmonic nanostructure acting as a dipolar emitter; (c) high electric near-field enhancement at the poles of the nanostructure [AG Fleischer; <http://www.silmeco.com/knowledge-base/hot-spots>]

Plasmon resonances of small spherical particles

[e.g. Benson p. 230, Maier p. 33, Novotny p. 392]

For the case of small spherical particles in the quasi-static approximation, the LSPP model can be analytically solved. A sphere of radius a in a uniform static electric field $\mathbf{E}_{in} = E_0 \mathbf{e}_z$ is assumed. The surrounding medium is isotropic and non-absorbing with a dielectric constant ϵ_d , and the metal sphere is described by a complex dielectric function ϵ_s . The electric field $\mathbf{E} = -\nabla\Phi$ can be obtained by solving the Laplace equation $\Delta\Phi = 0$. In spherical coordinates (r, θ, ϕ) the Laplace equation is of the form

$$\frac{1}{r^2 \sin \theta} \left[\sin \theta \partial_r (r^2 \partial_r) + \partial_\theta (\sin \theta \partial_\theta) + \frac{1}{\sin \theta} \partial_\phi^2 \right] \Phi(r, \theta, \phi) = 0 \quad (3.33)$$

Due to the azimuthal symmetry the general solution for the potential Φ is independent of ϕ and has the form

$$\Phi_s(r, \theta) = \sum_{l=0}^{\infty} A_l r^l P_l(\cos \theta) \quad (3.34)$$

$$\Phi_d(r, \theta) = \sum_{l=0}^{\infty} (B_l r^l + C_l r^{-l-1}) P_l(\cos \theta) \quad (3.35)$$

where P_l are the Legendre polynomials of order l , Φ_s is the potential inside the sphere, and $\Phi_d = \Phi_{scatter} + \Phi_0$ is the potential outside the sphere, consisting of an incoming and a scattered part.

When applying boundary conditions at the interface $r = a$ for the tangential component of the electric field ($\partial_\Theta \Phi_s = \partial_\Theta \Phi_d$ at $r = a$) and for the longitudinal component of the displacement field ($\epsilon_s \partial_r \Phi_s = \epsilon_d \partial_r \Phi_d$ at $r = a$), the potentials are evaluated to

$$\Phi_s(r, \Theta) = -\frac{3\epsilon_d}{\epsilon_s + 2\epsilon_d} E_0 r \cos \Theta \quad (3.36)$$

$$\Phi_d(r, \Theta) = -E_0 r \cos \Theta + \frac{\epsilon_s - \epsilon_d}{\epsilon_s + 2\epsilon_d} E_0 \frac{a^3}{r^2} \cos \Theta = -E_0 r \cos \Theta + \frac{\mathbf{p} \cdot \mathbf{r}}{4\pi\epsilon_0\epsilon_d r^3} \quad (3.37)$$

$$\text{with } \mathbf{p} = 4\pi\epsilon_0\epsilon_d a^3 \frac{\epsilon_s - \epsilon_d}{\epsilon_s + 2\epsilon_d} \mathbf{E}_0 \quad (3.38)$$

Here the **dipole moment** \mathbf{p} is introduced that is induced in the sphere by the external field. The light that is re-emitted by the small sphere can thus be approximated by a radiating dipole. The electric field can then be expressed as

$$\mathbf{E}_s = \frac{3\epsilon_d}{\epsilon_s + 2\epsilon_d} \mathbf{E}_0 \quad (3.39)$$

$$\mathbf{E}_d = \mathbf{E}_0 + \frac{1}{4\pi\epsilon_0\epsilon_d} \frac{3\mathbf{n}(\mathbf{n} \cdot \mathbf{p}) - \mathbf{p}}{r^3} \quad (3.40)$$

where $\mathbf{n} = \mathbf{r}/r$ is the unit vector in the direction of the point of interest.

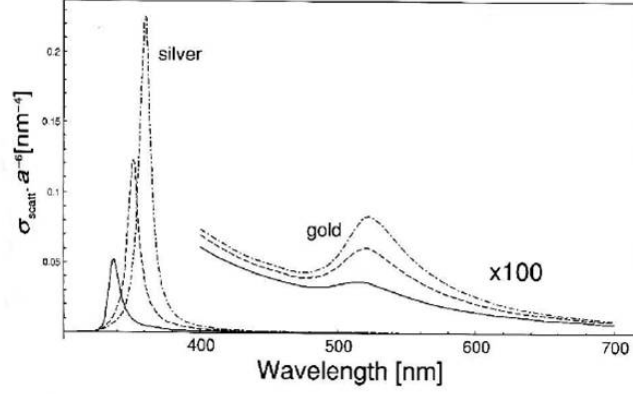


Fig. 3.13: Plots of the scattering cross-sections of spherical Ag and Au nanoparticles in different environments normalized by a^6 (a : particle radius); solid line: spheres in vacuum, $n = 1$, dashed line: in water, $n = 1.33$, dash-dotted line: in glass, $n = 1.5$ [Novotny and Hecht “Principles of Nano-Optics”, Cambridge University Press (2006)]

The **polarizability**, defined by the relation $\mathbf{p} = \epsilon_0 \epsilon_d \alpha \mathbf{E}_0$, then becomes

$$\alpha = 4\pi\epsilon_0 a^3 \frac{\epsilon_s - \epsilon_d}{\epsilon_s + 2\epsilon_d} \quad (3.41)$$

The scattering cross-section σ_{scat} of the sphere is then obtained by dividing the total radiated power of the dipole, $P = \omega^4 / (12\pi\epsilon_0\epsilon_d c^3) |\mathbf{p}|^2$, by the intensity of the exciting wave, $I = (1/2)c\epsilon_0\epsilon_d E_0^2$,

$$\sigma_{scat} = \frac{k^4}{6\pi\epsilon_0^2} |\alpha(\omega)|^2 = \frac{8\pi}{3} k^4 a^6 \left| \frac{\epsilon_s - \epsilon_d}{\epsilon_s + 2\epsilon_d} \right|^2 \quad (3.42)$$

Figure 3.13 shows plots of the (material dependent) normalized scattering cross-sections of silver and gold particles. A clear redshift (shift to longer wavelengths) of the resonance is observed when the dielectric constant of the dielectric environment is increased.

Power is lost from the incident beam due to the plasmons both by **scattering** and by **absorption**. The sum of the absorption and scattering is called **extinction**. From Poynting’s theorem, the power corresponds to that dissipated by a point dipole, i.e. $P_{abs} = (\omega/2)\text{Im}(\vec{\mu} \cdot \mathbf{E}_0^*)$. Using $\vec{\mu} = \epsilon_d \alpha \mathbf{E}_0$, the absorption cross-section becomes

$$\sigma_{abs} = \frac{k}{\epsilon_0} \text{Im}(\alpha(\omega)) = 4\pi k a^3 \text{Im}\left(\frac{\epsilon_s - \epsilon_d}{\epsilon_s + 2\epsilon_d}\right) \quad (3.43)$$

One can see that the scattering scales with a^6 , while the absorption process scales with a^3 . Consequently, for larger particles scattering dominates, whereas for smaller particles, extinction is dominated by absorption. The transition between the two regimes is characterized by a color change. For example small gold particles preferentially absorb green and blue light and thus appear reddish. On the other hand, larger gold particles (~ 80 nm) mostly scatter in the green and appear greenish. This effect is used in colored glasses as depicted at the beginning of the chapter.

The plasmon resonance (and therefore the “colour” of the nanoparticles) is influenced by several parameters and can be engineered accordingly, to e.g. match the particles to a particular laser wavelength or molecular transition. Some examples of the influence of different parameters on the resonance are depicted in Fig. 3.14.

- Choice of the nanostructure material (metal): The plasmon resonances e.g. for gold particles appear at longer wavelengths than for silver particles with the same size and geometry.
- Choice of dielectric medium: A surrounding medium with a higher dielectric constant leads to a shift of the plasmon resonance to longer wavelengths.
- Nanostructure geometry: Increasing the size shifts the plasmon resonance to longer wavelengths.
- Shape: Different shapes of the same volume result in different plasmon resonances.
- Aspect ratio: Elliptical particles show a **dichroism**, which means that one obtains two different resonances, one at a shorter and one at a longer wavelength, for excitation fields that are polarized parallel to the short and the long axis, respectively; the long axis resonance is further shifted to longer, and the short axis resonance to shorter wavelengths for increasing aspect ratio.

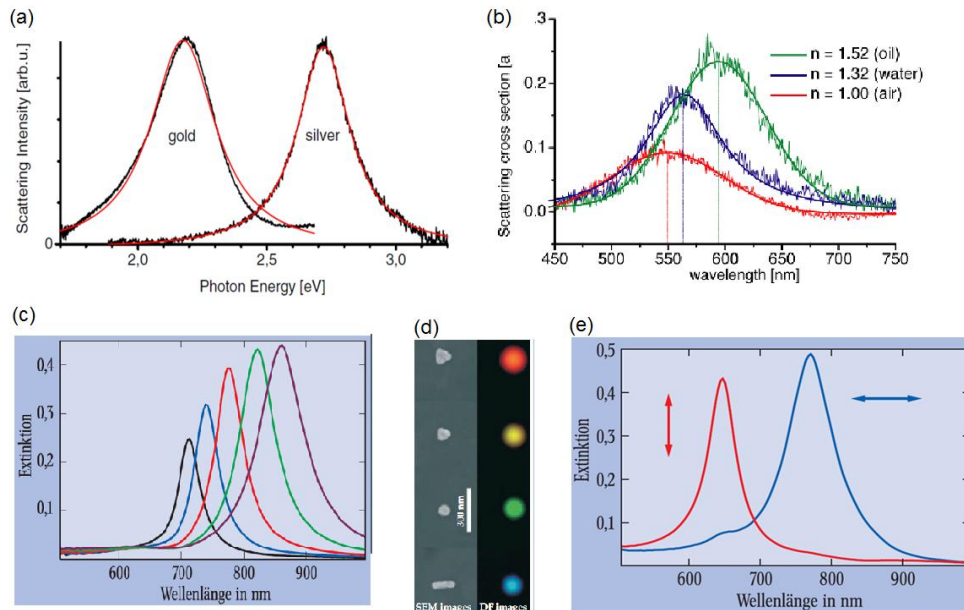


Fig. 3.14: Dependence of the plasmon resonance on different parameters: (a) Nanoparticle material (gold vs. silver) - note the axis: $E \propto 1/\lambda$; (b) embedding dielectric medium (air, water and oil); (c) particle size (40 nm high gold discs with diameters of 100 nm (black), 120 nm (blue), 140 nm (red), 160 nm (green), and 180 nm (purple)); (d) particle shape (colour of the resonance for triangles, discs, and nanorods); and (e) aspect ratio (long axis resonance (blue) and short axis resonance (red) for elliptical particles) [(a) C. Sönnichsen et al., New J. Phys. 4, 93 (2002); (b) P. Olk, Dissertation TU Dresden (2009); (c,e) J.R. Krenn et al., Physik Journal 1 (2002); (d) M.I. Stockman et al., Adv. Mater 19, 3771 (2007)]

3.5 Applications of plasmonics

3.5.1 Optical antennas

By concentrating the energy of the external electro-magnetic wave at the location of a nanoparticle or a tip, extremely localized, nanometer-scale light sources (scatterers) with a highly localized, highly enhanced electric near-field in the direct vicinity of the particle or tip surface are created. The external field induces oscillations of the free electron density in the nanostructure, which leads to a charge carrier flux. The structure in turn acts approximately as a point dipole and emits dipole radiation. These are typical characteristics of antenna behaviour. For this reason, metallic nanostructures with **plasmon resonances** in the ultraviolet/visible/near-infrared spectral range are also referred to as **optical antennas**.

Due to their properties as optical antennas and highly localized light sources, their high local electrical near-fields, and plasmon resonances that sensitively depend on external parameters, surface plasmon polaritons and plasmonic nanostructures are finding more and more practical application potential.

Such applications include:

- Surface and tip enhanced Raman scattering (SERS, TERS)
- Fluorescence enhancement
- SPP and LSPP sensors in biology, chemistry and medicine
- Optoelectronic devices (LEDs, solar cells)
- Information technology (signal transfer at the velocity of light)
- High-resolution optical near-field microscopy (SNOM)
- Near-field lithography
- Optical traps
- Plasmonic waveguides
- Local temperature increases (e.g. magnetic recording, water disinfection)
- Medical applications (e.g. non-bleaching labels, hyperthermal treatment)

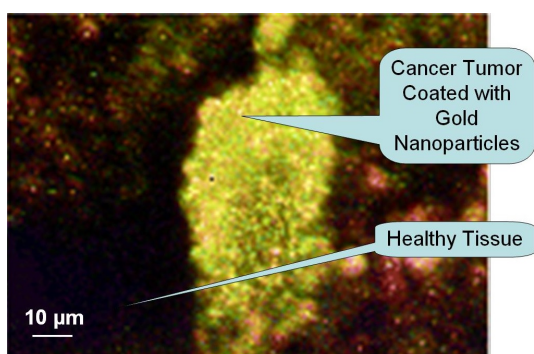


Fig. 3.15: Tumor cell with gold nanoparticles, which are functionalised with a recognition structure. Irradiation leads to a local increase in temperature and destruction of the tumor cell [P. M. Prajapati et al., J. Chem. Pharm. Res. 2(1), 30 (2010)].

3.5.2 Near-field scanning optical microscopy (NSOM/SNOM)

→ See also chapter ‘Characterization’

In near-field microscopy (*near-field scanning optical microscopy, NSOM/SNOM*), a sharp tip is brought into immediate vicinity of a surface by means of a feedback loop. The tip then couples with the evanescent near-field of the sample. Emitted photons are then either detected as propagating modes in a fiber (aperture NSOM) or scattered into the far-field by a massive metal tip or particle tip (apertureless NSOM), see Fig. 3.16. The achievable resolution of this technique corresponds to approximately the diameter of the tip or aperture respectively, and is thus far better than the confocal resolution of approximately $\lambda/2$.

During the last 10 years many tip designs based on localized plasmons were developed, with the aim of optimizing the probes for:

- light-harvesting efficiency (good antenna)
- smaller dimensions for higher resolution
- adjustable resonance frequencies or broadband excitation
- mechanical and chemical stability
- suitable polarization of the electric field

By SNOM the electric near-field at the surface, and therefore its optical properties are detected, which also means this technique enables the visualization of surface plasmons.

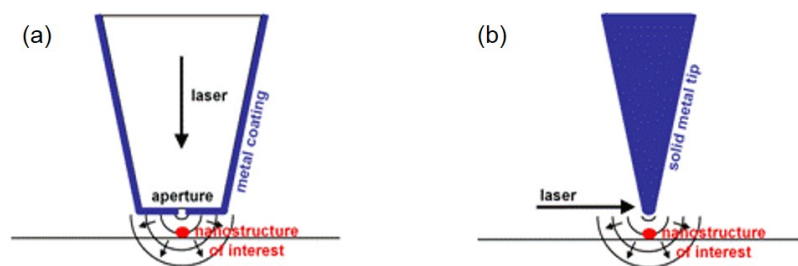


Fig. 3.16: Schematic representation of (a) aperture NSOM and (b) apertureless NSOM [<http://www.see.ed.ac.uk/cbee/SNOM1.html>]

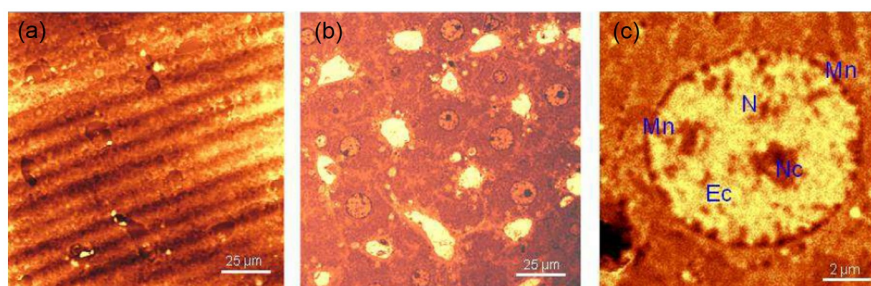


Fig. 3.17: (a) AFM and (b) transmission NSOM images with (c) a zoom into a histological microtome section of a rat liver; N Nucleus, NC Nucleolus, Ec Euchromatin, Hc Heterochromatin, and Mn cell membrane [Witec-Webinar (2010)]

3.5.3 Resonance shift sensors

a) SPP sensors

Principle: A gold-coated prism is illuminated in the Kretschmann configuration. At the resonance angle Θ_0 , SPPs are excited at the gold interface. If now a layer of molecules is adsorbed onto the surface, the effective refractive index of the medium close to the surface is increased, which shifts Θ_0 to a larger angle Θ_n . The shift $\Delta\Theta = \Theta_n - \Theta_0$ is then plotted vs. time. Flushing the surface with a buffer solution regenerates the surface, which restores the original angle Θ_0 .

SPP sensors can be applied as gas sensors or in flow cells. By functionalisation of the surface with molecular recognition structures the sensors can be made **specific** for certain analytes, e.g. as immunosensors according to the antigen-antibody detection principle.

SPP sensors are able to detect extremely small concentrations (sub-monolayers). They are commonly characterized in terms of

- RU (*resonance units*): 10^3 RU correspond to an angle change $\Delta\Theta = 0.1^\circ$, caused by a biomolecule concentration of $c = 1 \text{ ng/cm}^2$
- RIU (*refractive index units*): Used to describe the sensitivity $d\Theta/dn_{eff}$. Sensitivities up to $3 \cdot 10^{-7}$ RIU can be reached.

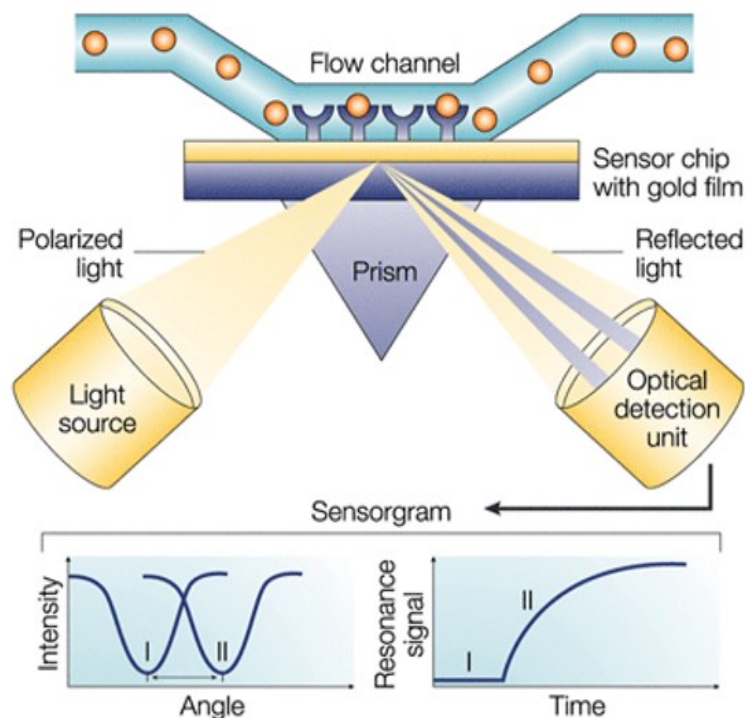


Fig. 3.18: Schematic of a surface plasmon sensor in a fluidic channel; bottom: shift of the resonance angle Θ_0 caused by attachment of molecules and plot of the angle shift versus time [M. A. Cooper, Nature Reviews Drug Discovery 1, 515 (2002)]

b) LSPP sensors

Principle: Nanostructures exhibit well-defined plasmon resonances. An adsorption of molecules changes the effective refractive index of the medium close to the surface. This leads to a shift of the resonance to longer wavelengths, which is denoted as $\Delta\lambda$ and plotted versus time. By functionalisation of the surface, specific detection is enabled in this case as well. The detection scheme is shown in Fig. 3.19.

The shift of the maximum λ_{max} of the resonance curve can be described as

$$\Delta\lambda_{max} = m\Delta n_{eff}(1 - e^{-2d/l_d}) \quad (3.44)$$

where m is the sensitivity of the nanoparticle (shift in nm per refractive index unit), Δn_{eff} the change of the effective refractive index, d the effective thickness of the adsorbed layer and l_d the decay length of the evanescent near-field.

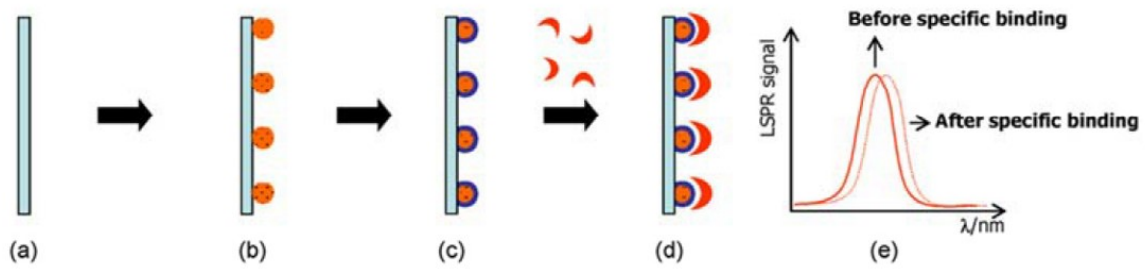


Fig. 3.19: LSPP sensor: (a) substrate, (b) optical antennas, (c) functionalisation with recognition structure, (d) accumulation of analyte molecules, (e) shift of the resonance wavelength due to specific binding [B. Sepulveda et al., Nano Today 4, 244 (2009)]

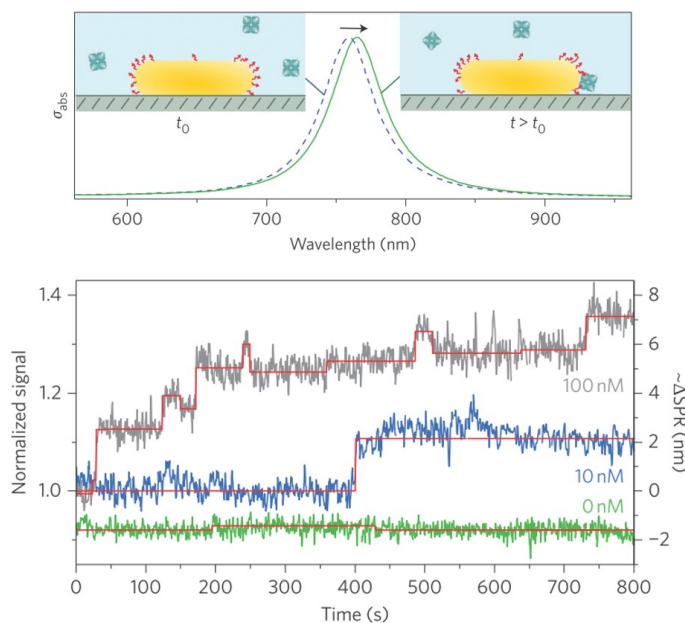


Fig. 3.20: LSPP sensor: (top) Resonance shift after adsorption of single molecules; (bottom) molecular dynamics in diagram of resonance shift plotted versus time [P. Zijlstra et al., Nature Nanotechnology 7, 379 (2012)]

3.5.4 Surface-enhanced Raman spectroscopy (SERS)

Principle: In surface-enhanced Raman spectroscopy, the locally enhanced near-field at single or between several optical antennas is used to increase the Raman intensity of individual molecules. For this purpose, these molecules must be placed in “hot-spots” of high field strength.

The enhancement factor EF is given as

$$EF_{SERS} = \frac{|E_{in}(\omega)|^2 |E_{out}(\omega - \omega_0)|^2}{E_0^4} \quad (3.45)$$

where E_0 is the field strength of the incoming electromagnetic wave, $E_{in}(\omega)$ the near-field enhanced field strength upon incidence on the nano structure, and $E_{out}(\omega - \omega_0)$ the Stokes-shifted, near-field enhanced field strength of the emitted light.

For nanoparticles in solution this enhancement can be expressed as

$$EF_{SERS} = \frac{I_{SERS}(\omega_\nu)/N_{surf}}{I_{NRS}(\omega_\nu)/N_{vol}}, \quad (3.46)$$

whereas at a surface, it is

$$EF_{SERS} = \frac{I_{SERS}(\omega_\nu)/A_{SERS}}{I_{NRS}(\omega_\nu)/A_0} \quad (3.47)$$

where I_{SERS} is the enhanced SERS intensity, I_{NRS} the regular, non-enhanced Raman intensity, N_{surf} the number of molecules bound to the particles, N_{vol} the total number of molecules in the excitation volume, A_{SERS} the area of hot-spots covered by molecules, and A_0 the focus area.

Areas of application: Detection of explosives and hazardous substances, drug detection, food safety, authenticity checks, biological research, environmental analysis: air and water quality, fire detection,

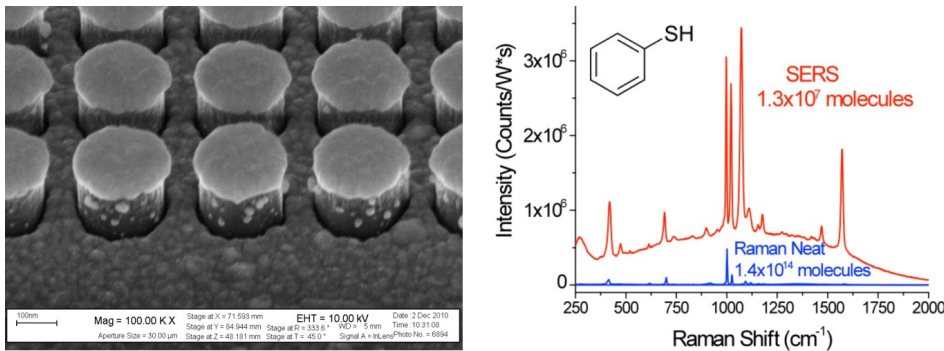


Fig. 3.21: Left: Example of a nanostructured SERS surface, scale: 100 nm; right: Raman signal of $1.4 \cdot 10^{14}$ thiophenol molecules without SERS substrate (blue), compared to the enhanced SERS signal of $1.3 \cdot 10^7$ molecules (red), enhancement factor $\sim 10^8$ [<http://www.nrl.navy.mil/media/news-releases/2011/>]

3.5.5 Tip-enhanced Raman spectroscopy (TERS)

→ See also chapter ‘Characterization’

Principle: In tip-enhanced Raman spectroscopy, instead of the near-field of a nanostructured surface, the electric near-field of a tip (scanning probe) is used to enhance the Raman signal. The experimental setup is similar to that of NSOM. The tip is scanned point-by-point across the surface, and a full enhanced Raman spectrum is recorded in each spot (*hyperspectral imaging* or *chemical mapping*). Subsequently images of the distribution of specific materials along the surface can be created by selecting characteristic Raman bands and spectrally filtering for these lines.

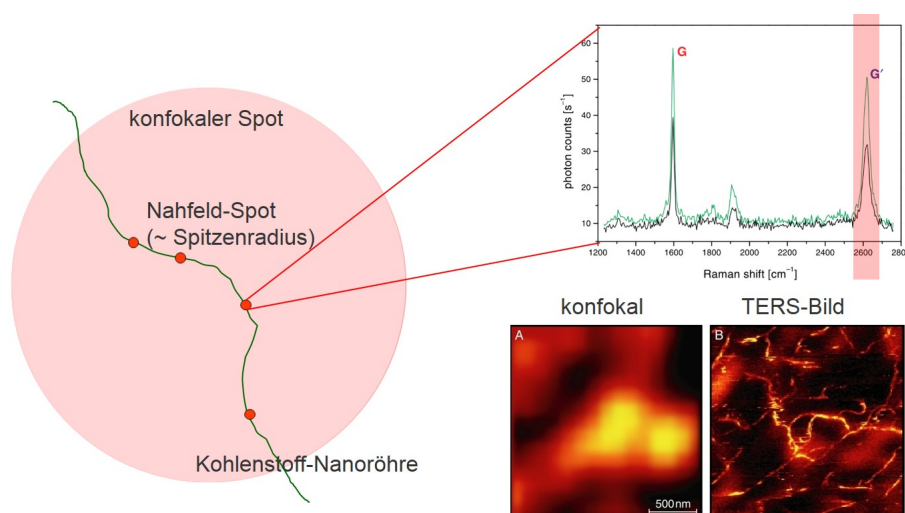


Fig. 3.22: Left: TERS scheme: The diffraction-limited spot is reduced to a spot of the size of the TERS tip. At each position of the sample a Raman spectrum is recorded (top right: Raman spectra of carbon nanotubes). From the intensity of the characteristic Raman bands it is then possible to reconstruct element specific images (bottom right: confocal vs. TERS images of CNTs [L. Novotny, University of Rochester])

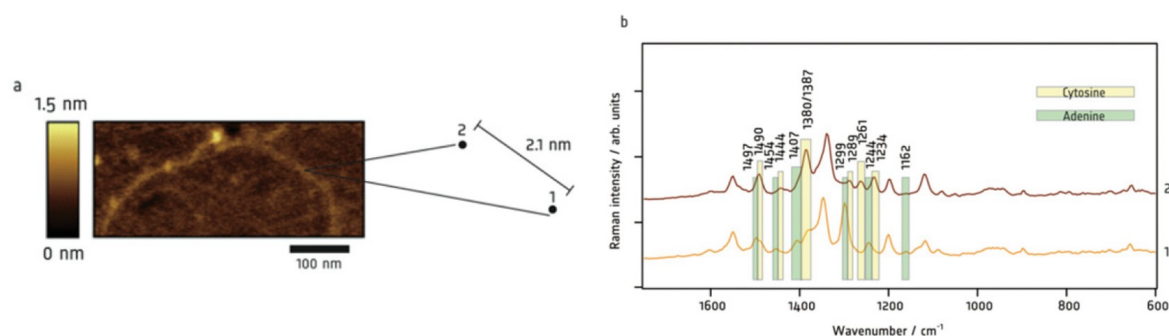


Fig. 3.23: TERS analysis of a DNA strand: Characteristic Raman spectra of different bases (spectrum 1: mostly cytosin, spectrum 2: mostly adenin) [R. Treffer et al., Biochem. Soc. Tran. 40, 609 (2012)]

3.6 Photonic crystals

Literature: L. Novotny and B. Hecht, *Principles of Nano-Optics*, Cambridge University Press (2006), p. 363-370; J.D. Joannopoulos, P.R. Villeneuve und S. Fan: *Photonic crystals: putting a new twist on light*, *Nature* 386, 143 (1997); L. Thylén, M. Qiu und S. Anand: *Photonic crystals - a step towards integrated circuits for photonics*, *ChemPhysChem* 5, 1268 (2004)

Photonic crystals are (usually artificial) structures with a **periodically varying dielectric constant** in one, two or three dimensions. The periodicity is below the wavelength of the incident light (e.g. for wavelengths of $\lambda \approx 1.5 \mu\text{m}$ periodicities of $\sim 500 \text{ nm}$). Under certain conditions it is possible for **photonic band gaps** to appear, i.e. frequency windows/wavelength ranges which cannot be scattered by the crystal (“forbidden frequencies”). The photonic band gaps for photons can be regarded analogous to electronic band gaps for electrons.

Goal:

Photonic crystals can suppress the propagation of light for certain wavelengths. This property makes them very interesting for photonic integrated circuits, since they allow for waveguiding, even around narrow bends, and make it possible to manipulate light.

Realisation:

In nature, photonic crystals occur as well in rare cases, e.g. in opals or the wings of certain butterflies (see Fig. 3.24). Artificial photonic crystals in 1D, 2D, or 3D can be manufactured through nanofabrication or self-assembly (see Fig. 3.25). First experimental realisations were demonstrated in the 1990s. Some examples are shown in Fig. 3.26.

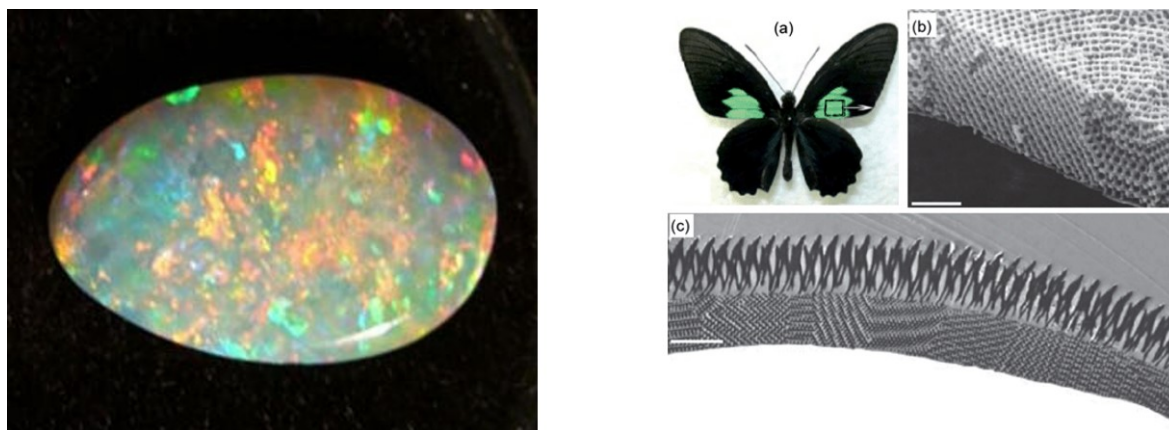


Fig. 3.24: Left: Opal as a naturally occurring photonic crystal; right: photonic crystal structure in butterfly wings [<http://daten.didaktikchemie.uni-bayreuth.-de/-umat/photon.effekt/opal.jpg>; S. Lou et al., *Energy Environ. Sci.*, 5, 9195 (2012)]

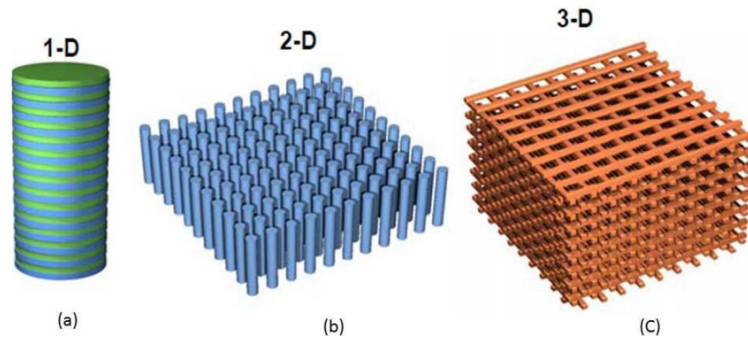


Fig. 3.25: Sketch of 1D, 2D, and 3D photonic crystals with periodically varying dielectric constants [S. Robinson et al., <http://dx.doi.org/10.5772/54533>]

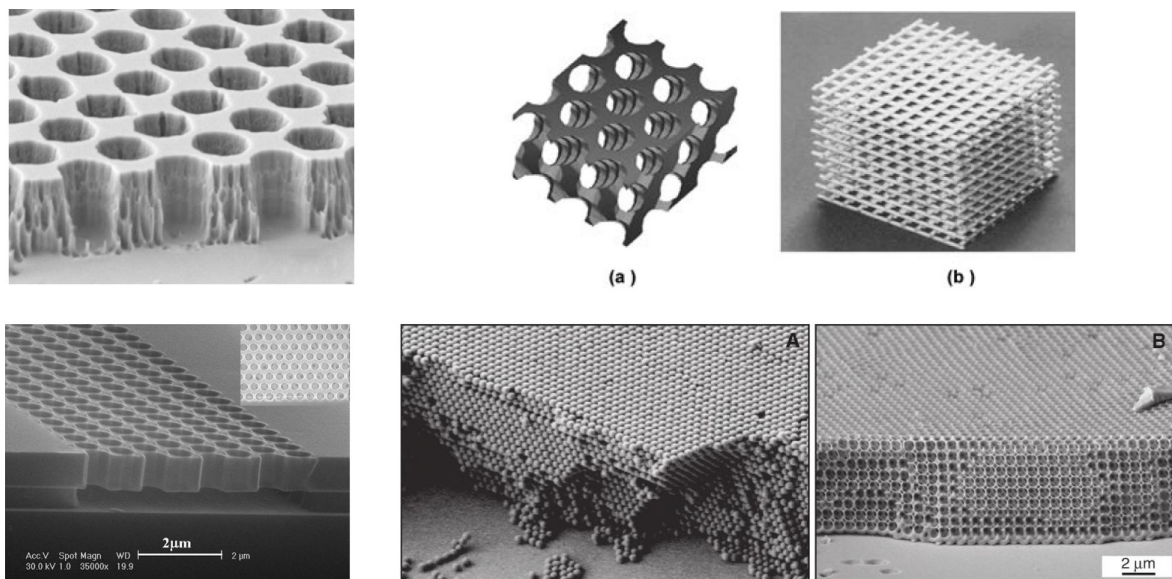


Fig. 3.26: Left: 2D crystals on a substrate and as a free-standing membrane; right: 3D crystals as inverse opals, woodpile structure, or opal consisting of small spheres [http://phys.org/news/2012-02-kind-high-temperature-photonic-crystal-power.html; C.S. Wu et al., doi:10.5772/8179 (2010); L. Thylen, ChemPhysChem 5, 1268 (2004); Novotny/Hecht, Cambridge University Press (2006)]

Calculating the photonic band gap:

The optical modes of the crystal can be calculated using the Maxwell equations for periodic dielectric media. For 1D crystals this can be done analytically (analogous to a Bragg lattice), but 2D and 3D crystals can only be solved numerically. The obtained solutions are **scalable**, which means that if the periodicity of the crystal is increased, the corresponding frequencies are increased by the same factor.

Calculating the 1D mode structure [cf. Novotny and Hecht, p. 363]:

Assumption: We consider a material consisting of an infinite amount of flat, non-magnetic, lossless layers of thickness d , which are oriented perpendicularly to the z -axis (unit vector in x -direction: n_x), with alternating dielectric constants ϵ_1 and ϵ_2 , and $\mu_1 = \mu_2 = 1$. The wave vector of light is $\mathbf{k} = (k_x, k_y, k_z)$, see Fig. 3.27.

We also define:

For TE modes (electric field \parallel interfaces): $\mathbf{E}(\mathbf{r}) = E(z) \exp(i(k_x x + k_y y)) \mathbf{n}_x$

For TM modes (magnetic field \parallel interfaces): $\mathbf{H}(\mathbf{r}) = H(z) \exp(i(k_x x + k_y y)) \mathbf{n}_x$

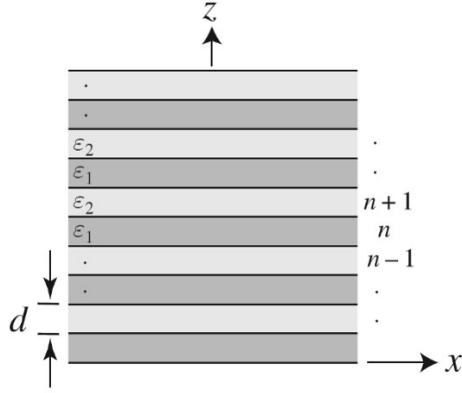


Fig. 3.27: Stack of layers with thickness d with alternating dielectric constants ϵ_1 and ϵ_2 [Novotny / Hecht, p. 363]

In each layer n we can then find solutions for $E(z)$ and $H(z)$, which are superpositions of a forwards and a backwards propagating wave:

$a_{n,j} \exp(ik_{zj}(z - nd)) + b_{n,j} \exp(-ik_{zj}(z - nd))$, with $a_{n,j}$ and $b_{n,j} = \text{const}(n, \epsilon_j)$.

Furthermore we define $k_{zj} = \sqrt{\frac{\omega^2}{c^2} \epsilon_j - k_{\parallel}^2}$ and $k_{\parallel} = \sqrt{k_x^2 + k_y^2}$.

At $z_n = nd$ the following boundary conditions hold:

TE: $E_{n,1}(z_n) = E_{n+1,2}(z_n)$ and $\frac{dE_{n,1}(z_n)}{dz} = \frac{dE_{n+1,2}(z_n)}{dz}$

TM: $H_{n,1}(z_n) = H_{n+1,2}(z_n)$ and $\frac{1}{\epsilon_1} \frac{dH_{n,1}(z_n)}{dz} = \frac{1}{\epsilon_2} \frac{dH_{n+1,2}(z_n)}{dz}$

Analogous boundary conditions apply for $z_{n-1} = (n-1)d$.

$a_{n-1,2}$ and $b_{n-1,2}$ can be linked to $a_{n+1,2}$ and $b_{n+1,2}$ using the **Floquet-Bloch theorem**: In a medium with periodicity $2d$, we find that: $E(z + 2d) = \exp(ik_B 2d) E(z)$, where k_B is the Bloch wave vector; $H(z)$ analogous.

From this one obtains $a_{n+1,2} = a_{n-1,2} \exp(ik_B 2d)$ and $b_{n+1,2} = b_{n-1,2} \exp(ik_B 2d)$.

There follows a homogeneous system of equations, of which the determinant must be zero. From this we then obtain the **characteristic equation**:

$$\cos(2k_B d) = \cos(k_{z1} d) \cos(k_{z2} d) - \frac{1}{2} \left(p_m + \frac{1}{p_m} \right) \sin(k_{z1} d) \sin(k_{z2} d) \quad (3.48)$$

with $p_m = \frac{k_{z2}}{k_{z1}}$ for TE modes and $p_m = \frac{k_{z2}}{k_{z1}} \frac{\epsilon_1}{\epsilon_2}$ for TM modes.

Since $\cos(2k_B d) \in [-1; 1]$, there are no solutions if the right side is > 1 , which is (analogously to electrons in an atomic lattice) the source of **photonic band gaps**. This is schematically shown in Fig. 3.28.

In the energy diagram of the dispersion relations $\omega(k_{\parallel})$ one can see allowed bands of frequencies that can propagate through the crystal, and bands of forbidden frequencies. The results of the calculations for TE and TM modes are shown in Fig. 3.29.

1D crystals do not show a **complete band gap**, which means there are no frequencies at which propagation is forbidden in all directions (see Fig. 3.29(a)).

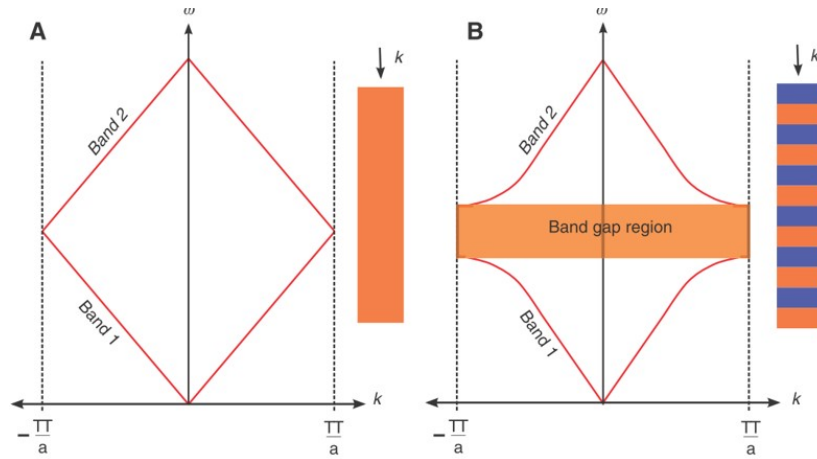


Fig. 3.28: Sketch of the generation of a photonic band gap when a material is structured as a Bragg grating.

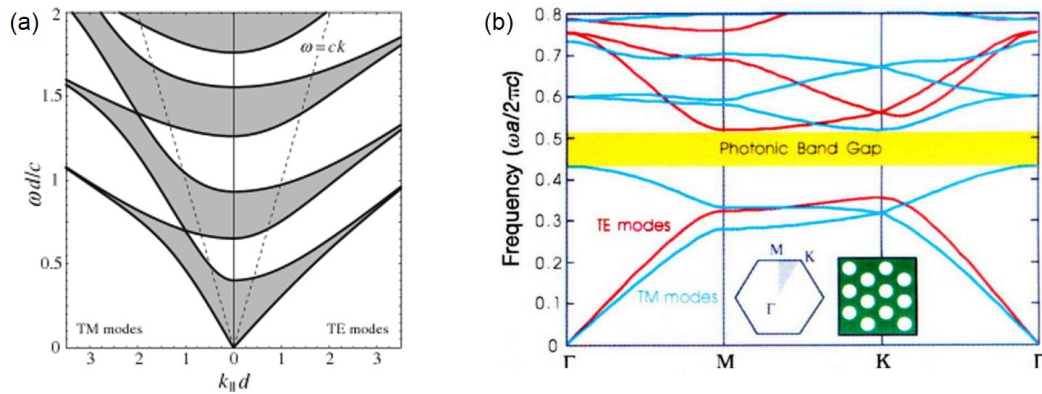


Fig. 3.29: (a) Energy diagram of the TE and TM modes in a 1D photonic crystal; the gray areas represent allowed bands; (b) Band diagram of a 2D triangular lattice of air cylinders in a dielectric ($\epsilon = 13$), showing a complete photonic band gap [Novotny/Hecht, Cambridge University Press (2006); J.D. Joannopoulos et al., Nature 386, 143 (1997)]

However, waves impinging from the vacuum can only excite modes with $k_{\parallel} < \frac{\omega}{c}$, which also have complete band gaps (see Fig. 3.29). This results in 1D crystal **perfect mirrors**, or omni-directional reflectors.

In 3D it is generally possible to observe complete band gaps, especially at high contrasts $\epsilon_2 \gg \epsilon_1$.

In the **dielectric band** (which corresponds to the valence band), the optical energy is confined to the material which has the higher ϵ , whereas in the **air band** (corresponding to the conduction band) it is localized in the material with lower ϵ .

Defects:

The suppression of light propagation can locally be canceled with the help of crystal defects (see Fig. 3.30 and 3.31). This allows for light to be localized or directed. As a result, photons with energies within the photonic band gap cannot propagate through the crystal, but instead through defect lines.

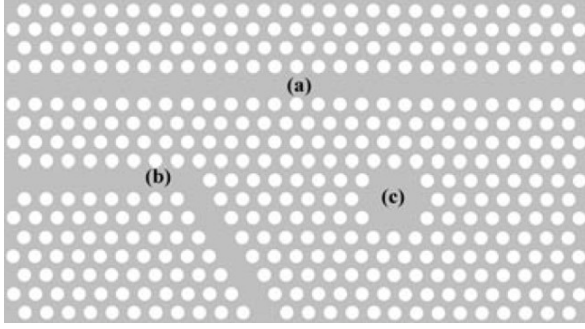


Fig. 3.30: (a,b) Line defects, (c) point defect (*cavity*) [L. Thylen, ChemPhysChem 5, 1268 (2004)]

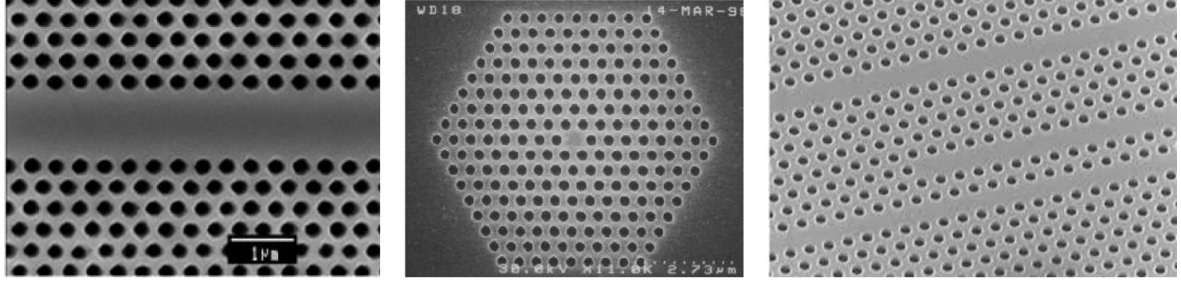


Fig. 3.31: 2D waveguide and point resonator in photonic crystals [L. Thylen, ChemPhysChem 5, 1268 (2004); Y. Takahashi, www.pro-physik.de (26.6.2013)]

- **2D: Planar defects** fully reflect light and can be considered as perfect mirrors.
- **1D: Line defects** serve as waveguides for photonic modes. Implementations of line defects and a simulation of the corresponding waveguide can be seen in Fig. 3.32.
- **0D: Point defects** act as micro-cavities and thus as resonators with a very high **Q factor** (quality factor) $Q = \omega_0 / \Delta\omega$, where ω_0 is the resonance frequency and $\Delta\omega$ the full-width-at-half-maximum of the resonance. Such localized defects are used for *light trapping*, whereby the spontaneous emission rate of quantum systems (atoms, molecules, quantum dots, nitrogen-vacancy (NV-)centers) at the position of the defect can be strongly increased. The spontaneous decay rate is increased by a factor of

$$K = \frac{D}{8\pi} Q \frac{\lambda_0^3}{V} \quad (3.49)$$

where V is the volume of the cavity, λ_0 the emission wavelength within the respective material, and D the mode degeneracy (number of modes with the same frequency within the cavity). $K = \rho_c / \rho_f$ reflects the relation of the density of states within the cavity ρ_c and the free density of states ρ_f . Up to a pre-factor this corresponds to the **Purcell factor** F_P , which describes the enhancement of spontaneous emission rates of an atom within a resonant cavity:

$$F_P = \frac{3}{4\pi^2} \left(\frac{\lambda_c}{n} \right)^3 \left(\frac{Q}{V} \right) \quad (3.50)$$

By utilizing small cavities and high Q factors it is possible to strongly enhance the emission.

Possible applications:

Waveguides with nearly lossless guidance around narrow bends, lasers, optical filters / filter couplers, LEDs, super-prisms with high non-linear dispersion, negative refraction, manipulation and control of spontaneous emission in quantum systems.

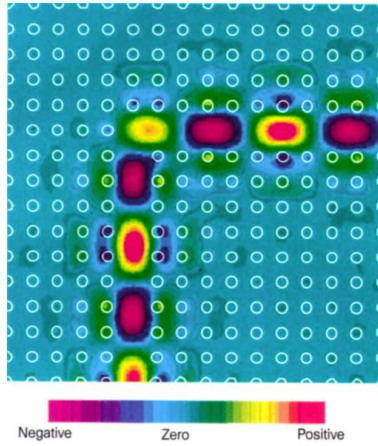


Fig. 3.32: Electric field distribution of light propagating through a wave guide along a narrow bend [J.D. Joannopoulos et al., Nature 386, 143 (1997)]

3.7 Metamaterials

Literature: [W. Cai and V. Shalaev, *Optical Metamaterials - Fundamentals and Applications*, Springer (2010); D. Schurig et al., *Science* 314, 977 (2006); J. Valentine et al., *Nature* 455, 376 (2008)]

Metamaterials are artificial materials which exhibit electromagnetic inhomogeneities. Spatial variations of the electromagnetic parameters $\epsilon(\vec{r})$, $\mu(\vec{r})$ on the sub-wavelength scale lead to distortions of \vec{D} , \vec{B} and the Poynting vector \vec{S} , caused by coordinate transformations, see the schematic in Fig. 3.33. For this reason, this research area is also called **transformation optics**. It allows for the generation of properties that are not observed in naturally occurring materials.

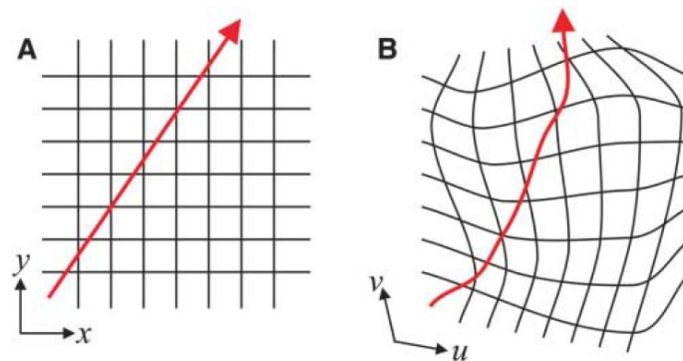


Fig. 3.33: (a) Field line in free space on a Cartesian coordinate grid, (b) distorted field line with equally distorted background coordinates [J.B. Pendry et al., *Science* 312, 1780 (2006)]

a) Invisibility cloaks for certain frequency ranges:

Ansatz: The space of the volume of an object is transformed onto an envelope around the object. A coordinate transformation $\vec{x} \rightarrow \vec{u}$ leaves the Maxwell equations unchanged, but modifies ϵ and μ as a function of $(\partial x_i / \partial u_j)$. As a result, beams are redirected around the object and it becomes “invisible”.

Ex. 1: Transformation for a sphere with radius R_1 ; $r < R_2 \rightarrow R_1 < r < R_2$

Transformation: $r' = R_1 + r(R_2 - R_1)/R_2$, $\Theta' = \Theta$, $\Phi' = \Phi$

In the range $R_1 < r < R_2$ this then yields:

$$\epsilon'_{r'} = \mu'_{r'} = \frac{R_2}{R_2 - R_1} \frac{(r' - R_1)^2}{r'}; \quad \epsilon'_{\Theta'} = \mu'_{\Theta'} = \epsilon'_{\Phi'} = \mu'_{\Phi'} = \frac{R_2}{R_2 - R_1} \quad (3.51)$$

and for $r > R_2$: $\epsilon'_{r'} = \mu'_{r'} = \epsilon'_{\Theta'} = \mu'_{\Theta'} = \dots = 1$

Fig. 3.34 illustrates the beam path around the sphere.

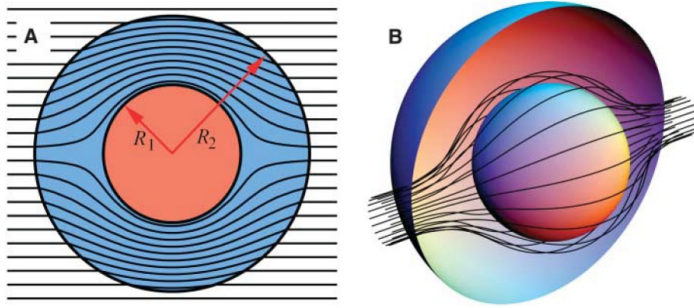


Fig. 3.34: Transformation optics directs linear beams around a sphere [J.B. Pendry et al., Science 312, 1780 (2006)]

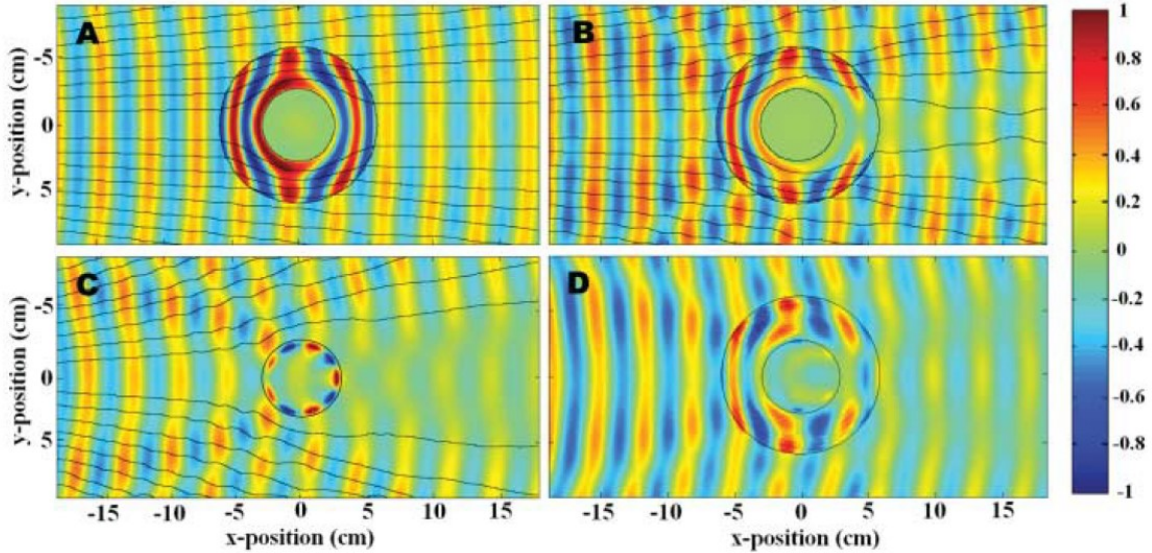


Fig. 3.35: Electric field distributions with beam paths (in the direction of the Poynting vector) for a ring-shaped invisibility cloak around a conducting copper cylinder. (a) Simulation using exact material properties, (b) simulation of the invisibility cloak with reduced material properties, (c) experimental measurement of the conducting cylinder, (d) measurement of the cloaked cylinder [D. Schurig et al., Science 314, 977 (2006)].

Ex. 2: Transformation of a cylinder, $0 < r < b \rightarrow a < r' < b$

Transformation: $r' = \frac{(b-a)r}{b} + a$, $\Theta' = \Theta$, $z' = z$

$$\epsilon_r = \mu_r = \frac{(r-a)}{r}, \quad \epsilon_\Theta = \mu_\Theta = \frac{r}{(r-a)}, \quad \epsilon_z = \mu_z = \left(\frac{b}{b-a}\right)^2 \frac{(r-a)}{r} \quad (3.52)$$

Rotational symmetry around E_z means that essentially only ϵ_z , μ_r , and μ_Θ are relevant. In 2006 a Cu cylinder was realized in a metamaterial as an invisibility cloak for the microwave range. Variation of ϵ and μ was implemented by using split-ring resonators (LC elements), see Fig. 3.36.

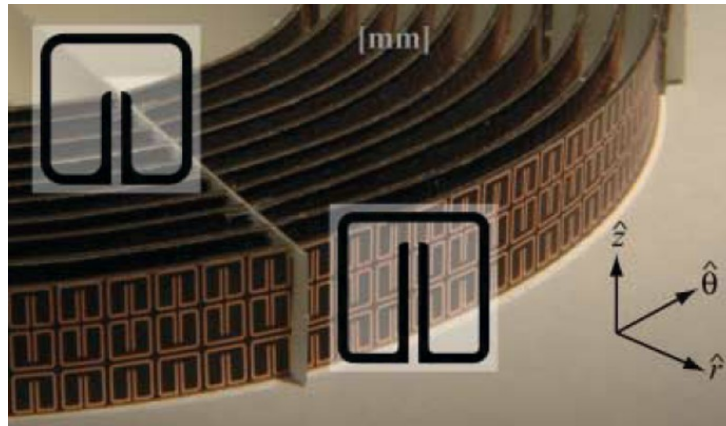


Fig. 3.36: Cylindrical invisibility cloak made of LC split-rings [D. Schurig et al., Science 314, 977 (2006)]

b) Negative refractive index $n < 0$:

In 1968 V. Veselago formulated the theory of negative refraction, which was first experimentally verified in the early 2000s. Artificial materials with $\epsilon < 0$ and $\mu < 0$ are able to refract light negatively. One possible realization are fishnet structures (coupled LC resonators), see Fig. 3.37 and 3.38.

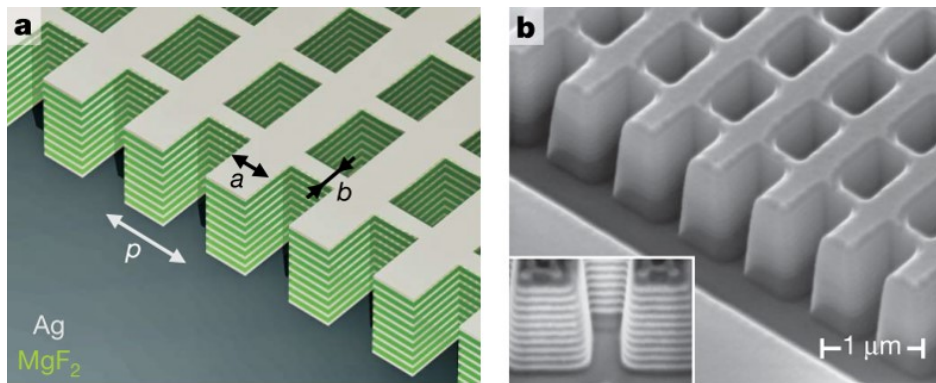


Fig. 3.37: Fishnet structure of a metamaterial with negative refractive index [J. Valentine et al, Nature 455, 376 (2008)]

Fig. 3.38 (top left) shows the schematic setup of a prism experiment. No refraction occurs at positions at which the incident light can propagate straight through the holes of the fishnet structure. For refractive indices $n > 0$ one would expect refraction to the left of the surface normal (angle β), while for negative refractive indices the light is refracted to the same side of the surface normal as the incident light (angle α). In Fig. 3.38 (top right) the simulation of a negative phase is shown, which leads to negative refraction. Fig. 3.38 (bottom left) shows the increasing shift of the refracted beam inside the structure. For increasing wavelengths the beam is initially shifted towards the surface normal and then away from it. The relationship between wavelength and refractive index, as well as the transition towards negative refractive indices is shown in Fig. 3.38 (bottom right).

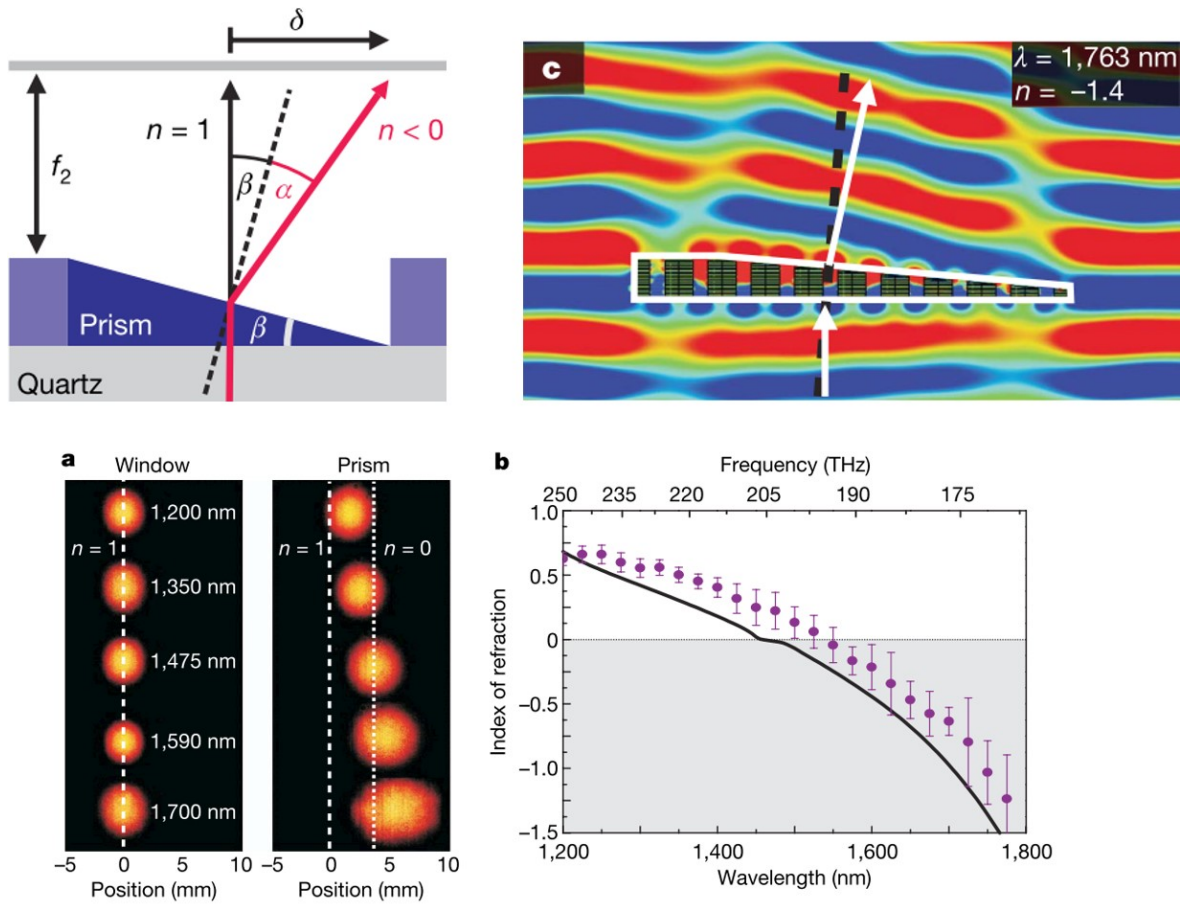


Fig. 3.38: Top left: Sketch of a prism with positive or negative refractive index, respectively; top right: negative phase upon passage through the metamaterial; bottom left: positive refraction of light through holes in the fishnet structure with $n = 1$, and increasing shift for increasingly negative refractive index for increasing wavelengths; bottom right: wavelength-dependent experimental and theoretical values of the refractive index [J. Valentine et al., Nature 455, 376 (2008)].

3.8 Single-photon emitters

Literature: e.g. [B. Lounis and M. Orrit, Single-photon sources, Rep. Prog. Phys. 68, 1129 (2005); M.D. Eisaman et al., Single-photon sources and detectors, Rev. Sci. Instr. 82, 071101 (2011)]

Photons can be seen as elementary excitations of single modes of the quantized electromagnetic field. An ideal single-photon state would have photon statistics with a mean value of 1 and a variance of 0.

Since ca. 1990 there is an increasing interest in single-photon sources, since they are of fundamental importance for many modern physical applications, e.g.

- Quantum-information processing
- Quantum-cryptography
- Photonic qubits
- Experimental quantum mechanics and quantum electrodynamics
- Single-photon microscopy

However, single photons are hard to implement. Even at extremely reduced intensities conventional light sources do not provide reliable single-photon sources. Examples of the emission statistics of thermal and coherent light sources with a mean emission count of $\langle n \rangle = 1$ photon are shown in Fig. 3.39. For comparison the figure also shows the statistics of an ideal single-photon source. The differences are due to interactions between the photons, which lead to the emission of wave packets.

To probe whether single photons are present, techniques for observing **antibunching** were developed: The emission of one photon rules out the simultaneous emission of a second one. An excited state cannot be excited a second time during its lifetime (typically on the order of ns), which means that only a single photon is emitted during this lifetime.

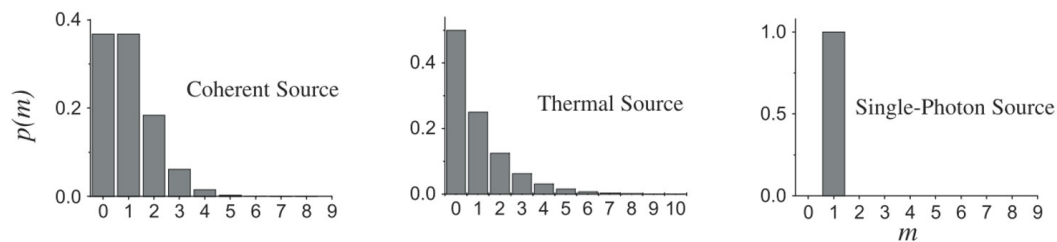


Fig. 3.39: Probability distributions of the numbers of emitted photons for three sources with a mean photon count $\langle n \rangle = 1$: coherent source with Poisson statistics, thermal source with Bose-Einstein statistics, and an ideal single-photon source [B. Lounis, M. Orrit, Rep. Prog. Phys. 68, 1129 (2005)]

In a cavity ($V = L^3$) the mode of the electric field is quantized as a harmonic oscillator, $\vec{E}(\vec{r}) = \vec{E}^-(\vec{r}) + \vec{E}^+(\vec{r})$ becomes an operator.

The **second-order correlation function** is defined as

$$\text{classical: } g^{(2)}(\tau) = \frac{\langle I(t+\tau)I(t) \rangle}{\langle I(t) \rangle^2}$$

$$\text{QM: } g^{(2)}(\tau) = \frac{\langle E^-(t)E^-(t+\tau)E^+(t+\tau)E^+(t) \rangle}{\langle E^-(t)E^+(t) \rangle^2}$$

A **Hanbury-Brown-Twiss interferometer** works by splitting the photon field using a beam splitter and detecting both halves individually. The wave function of a single photon must then collapse at one of the detectors. To measure this reliably it is necessary to use extremely sensitive detectors, e.g. **photomultiplier tubes (PMTs)** or **avalanche photo-diodes (APDs)**. The experimental setup is shown in Fig. 3.40.

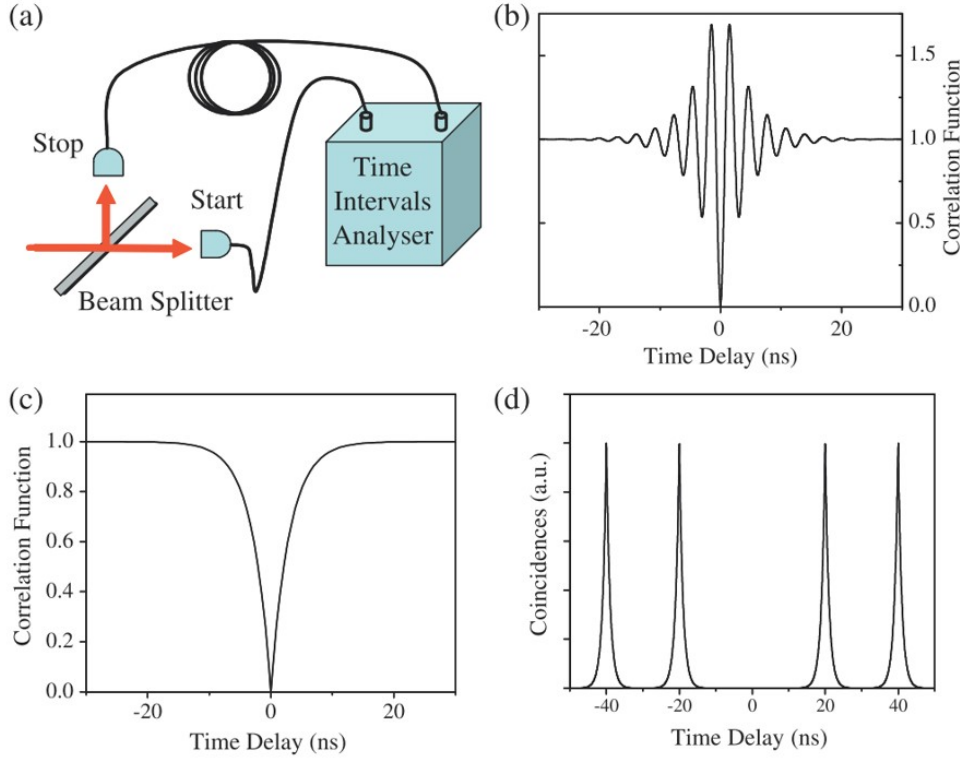


Fig. 3.40: (a) Schematic setup of a Hanbury-Brown-Twiss experiment; coincidences between events at both detectors result in a correlation function; (b) Rabi oscillations occur around the antibunching dip at long coherent lifetimes and high resonant excitation intensities; (c) for non-resonant excitations or very short lifetimes only a minimum occurs; (d) pulsed excitation leads to periodic emission of single photons, the peak at zero delay is suppressed due to antibunching [B. Lounis, M. Orrit, Rep. Prog. Phys. 68, 1129 (2005)]

For the case of ideal antibunching it holds: $g^{(2)}(0) = 0$, $g^{(2)}(\tau) > g^{(2)}(0)$.

If the time delay between the measurements at the two detectors is zero, a photon can only be observed at one of them; there can be no simultaneous signal at the other detector, which means the correlation of both signals is zero. If this time delay is increased there is also a higher probability to observe one photon each at both detectors. The rise time is characteristic for the lifetime of a given excited state. The second-order correlation approaches a constant value for increasing delay times.

Fig. 3.40(b) shows Rabi oscillations, which can be observed for long coherent lifetimes and high resonant excitation intensities. Fig. 3.40(c) shows an ideal correlation measurement with perfect antibunching at delay 0. Fig. 3.40(d) depicts the same experiment, but with pulsed excitation. A finite correlation is observed for delay times of the measurements at both detectors of > 0 pulse lengths. Antibunching is again observed for delay time 0, leading to a disappearance of the correlation peak at $\tau = 0$.

Fig. 3.41 shows experimental measurement curves of the correlation function for continuous and pulsed operation. In practice one assumes single-photon emission if the correlation at $\tau = 0$ is lower than $\sim 50\%$.

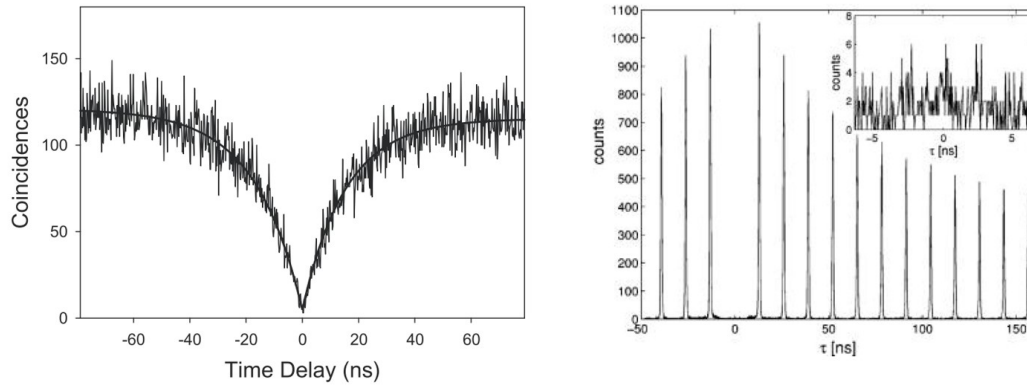


Fig. 3.41: Left: Measurement curve of the correlation function for continuous excitation, showing the antibunching dip; right: oscillations of the correlation due to pulsed excitation, missing antibunching peak [B. Lounis, M. Orrit, Rep. Prog. Phys. 68, 1129 (2005)]

An **ideal single-photon source** should have the following (experimentally almost impossible to realize) properties:

- Ability to emit exactly one photon when needed (“on demand”)
- 100% probability of single photon emission, no exceptions
- 0% probability of emitting multiple photons
- Photons indistinguishable (constant energy etc.)
- Ultra-fast, tunable repetition rates
- Constant time delay between excitation and emission
- Operation at room temperature and ambient conditions

Nano-realizations of single-photon sources (SPS):

In the search for single-photon sources, one is looking for two-level systems with an external control over the population of an excited state, which returns to a lower state or the ground-state upon emission of a photon (see Fig. 3.42). For this purpose, nano-objects with discrete energy level systems are employed. Some such examples are shown in Fig. 3.43.

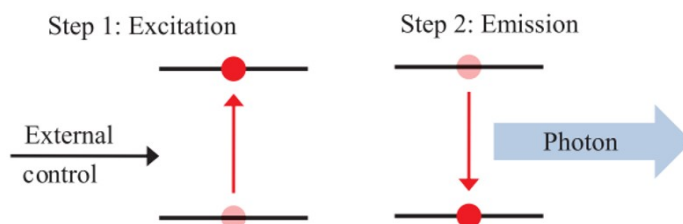


Fig. 3.42: Diagram of external excitation of a two-level system with subsequent photon emission [M.D. Eisaman et al., Rev. Sci. Instrum. 82, 071101 (2011)]

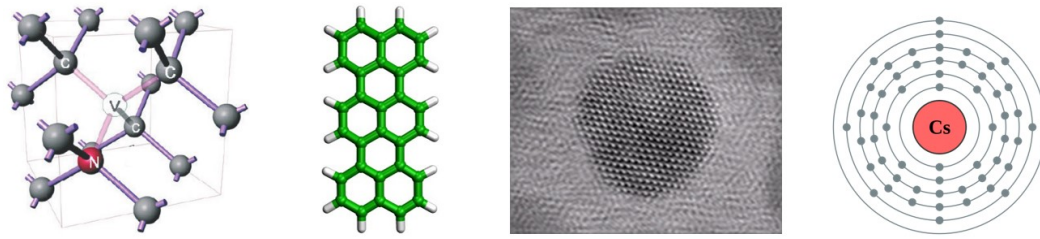


Fig. 3.43: Examples of nano-scale single photons sources (left to right): Diamond with NV colour center, Terrylene molecule, CdSe/ZnS quantum dot, Cs atom [B. Lounis, M. Orrit, Rep. Prog. Phys. 68, 1129 (2005); <http://gerhardt.ch/images/sms04.jpg>; T. Palucka, materials360online, Mat. Res. Soc., 13.2.2013]

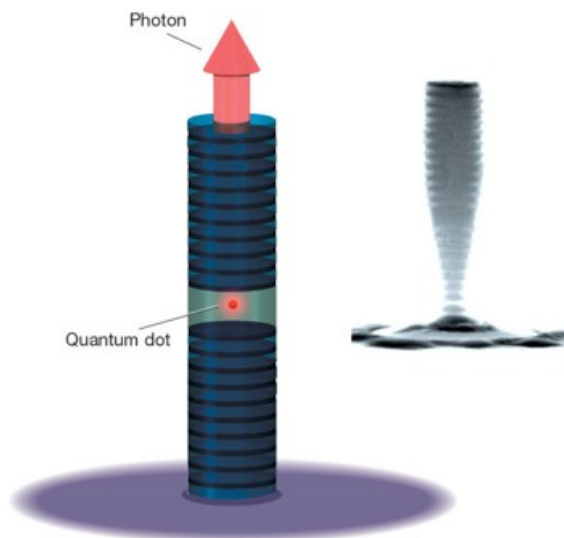


Fig. 3.44: Single-photon emitter in a 1D resonator (Bragg mirror; schematic and experimental structure): directional enhanced emission [K.J. Vahala, Nature 424, 839 (2003)]

a) **Deterministic SPS:** Single photons upon external excitation

- Colour centers in a nano-diamond, e.g. NV centers (*nitrogen vacancy*, where two C atoms are substituted by an N atom and an accompanying vacancy)
- Semiconductor quantum dots (GaN, InAs, CdSe/ZnS,...): Exciton transitions can be initiated by optical or electric excitation at cryogenic temperatures.
- Single atoms, single ions, ensembles of atoms (e.g. Rb, Cs): These provide electronic eigenstates, hyperfine structure, known energies, and small linewidths.
- Single molecules (dibenz-anthracene, terrylene, ...): At low temperatures, the zero-phonon line of transitions between vibrational ground states of the electric ground and excited states can be excited.

In addition, the above systems are often coupled to a resonator (*cavity*, see Fig. 3.44) in order to enhance spontaneous emission, out-couple radiation into a certain direction, and/or gain spectral control.

b) Probabilistic photon pairs: Random emission of entangled photon pairs from crystals, waveguides, or fibers, that are often used in quantum optics experiments.

